molecules

MDPI

Review

MoS_2 and MoS_2 Nanocomposites for Adsorption and Photodegradation of Water Pollutants: A Review

Leonardo O. Amaral and Ana L. Daniel-da-Silva *

Department of Chemistry and CICECO-Aveiro Institute of Materials, University of Aveiro, 3810-193 Aveiro, Portugal
* Correspondence: ana.luisa@ua.pt

Abstract: The need for fresh and conveniently treated water has become a major concern in recent years. Molybdenum disulfide (MoS_2) nanomaterials are attracting attention in various fields, such as energy, hydrogen production, and water decontamination. This review provides an overview of the recent developments in MoS_2-based nanomaterials for water treatment via adsorption and photodegradation. Primary attention is given to the structure, properties, and major methods for the synthesis and modification of MoS_2, aiming for efficient water-contaminant removal. The combination of MoS_2 with other components results in nanocomposites that can be separated easily or that present enhanced adsorptive and photocatalytic properties. The performance of these materials in the adsorption of heavy metal ions and organic contaminants, such as dyes and drugs, is reviewed. The review also summarizes current progress in the photocatalytic degradation of various water pollutants, using MoS_2-based nanomaterials under UV-VIS light irradiation. MoS_2-based materials showed good activity after several reuse cycles and in real water scenarios. Regarding the ecotoxicity of the MoS_2, the number of studies is still limited, and more work is needed to effectively evaluate the risks of using this nanomaterial in water treatment.

Keywords: molybdenum disulfide; nanocomposites; adsorption; photocatalysis; organic contaminants; heavy metal ions

check for updates

Citation: Amaral, L.O.; Daniel-da-Silva, A.L. MoS_2 and MoS_2 Nanocomposites for Adsorption and Photodegradation of Water Pollutants: A Review. *Molecules* **2022**, *27*, 6782. https://doi.org/10.3390/molecules27206782

Academic Editor: Minas M. Stylianakis

Received: 20 September 2022
Accepted: 7 October 2022
Published: 11 October 2022

Publisher's Note: MDPI stays neutral with regard to jurisdictional claims in published maps and institutional affiliations.

Copyright: © 2022 by the authors. Licensee MDPI, Basel, Switzerland. This article is an open access article distributed under the terms and conditions of the Creative Commons Attribution (CC BY) license (https://creativecommons.org/licenses/by/4.0/).

1. Introduction

The world's population has been growing yearly, and an increased need for resources has accompanied this growth [1]. Industrial, agricultural, and medical development have evolved to supply this population growth [1,2]. However, after this substantial increase in resource consumption, pollution had also increased, becoming a huge concern, along with the need for freshwater sources or for effective water treatment [1,3]. In this regard, several approaches for water treatment have been developed, such as adsorption and photocatalysis, to remove pollutants and other threats to human health and ecosystems, such as heavy metals, dyes, drugs, and pesticides, among others [4–8].

Along with the advances in environmental research, in the past few years, several authors have suggested nanomaterials to enhance primary and advanced water treatment [9]. Due to its small size and, consequently, high surface and reactive areas, the use of nanomaterials enables the improvement of several properties compared to bulk material [9]. More recently, two-dimensional (2D) nanomaterials have gained importance. In this group are included materials such as graphene, hexagonal boron nitride, 2D honeycomb silicon, and transition metal dichalcogenides (TMD) such as molybdenum disulfide (MoS_2) and tungsten disulfide (WS_2) [10]. TMD are hexagonal, structured and layered materials with the molecular formula MX_2, where M is a transition metal (Mo, W, or Nb) and X represents a chalcogen element (S, Se, or Te) [11,12]. Within this group of materials, nano-MoS_2 has gained attention year after year due to its outstanding chemical, electronic, catalytic, optical, and mechanical properties, making it suitable for various fields such as pollution

remediation and sensors, medicine, mechanics and electronics, and energy conversion and storage [13–24]. When compared to other sulfides, such as zinc sulfide (ZnS), cadmium sulfide (CdS), and tungsten sulfide (WS_2), MoS_2 show promising photocatalytic activity, allied to its easy preparation and unique optical and electronic properties [25]. The wide band gaps of ZnS and MnS render them responsive to only UV light; further modification is required to extend the light absorption range [26]. In contrast, MoS_2 is active with visible light. As a photocatalytic material, MoS_2 presents a suitable surface area with a large number of active site edges, a layered structure that allows good adsorption capacity, and a tunable band gap between 1.2 eV and 1.9 eV, depending on the number of layers [27]. Regarding safety considerations, Mo is less hazardous and can be used to substitute Cd, which is known to be a human carcinogen.

In this review, we first summarize the main structures and properties of MoS_2 and the most common methods by which to prepare MoS_2-based materials. We then critically review the recent advances in MoS_2-based materials for water treatment and purification through adsorption and photocatalysis.

2. MoS_2 Structure and Properties

In nature, MoS_2 exists in molybdenite bulk mineral form as a black powder [28]. Bulk MoS_2 can be exfoliated, obtaining few-layer nanosheets ($FLMoS_2$) and single-layer nanosheets ($SLMoS_2$) [29,30]. $SLMoS_2$ compared to bulk MoS_2 has intrinsic higher electronic conductivity and presents a direct gap of 1.7–1.9 eV, while bulk MoS_2 presents an indirect band gap of 1.1–1.3 eV [31–34]. This relatively small band gap of $SLMoS_2$ enables the use of visible light to perform photocatalytic reactions [35,36]. While absent in the bulk material, $SLMoS_2$ also shows strong photoluminescence [37]. At room temperature, $SLMoS_2$ exhibits an on/off current ratio of 10^8 and an electron mobility of 200 cm^2 $(V.s)^{-1}$ [38]. Notably, several properties of MoS_2 can be adjusted by varying the number of layers and polymorphism. $SLMoS_2$ presents a sandwich structure with a thickness of 0.6 nm, composed of two layers of atomic S, with a single layer of atomic Mo between, linked through Mo-S covalent bonds [39–41]. In the case of $FLMoS_2$, the different sheets interact with each other via weak van der Waals (vdW) forces [40,42]. Because of these weak vdW forces, changing $SLMoS_2$ to $FLMoS_2$ and gaining the reverse reaction is easily achieved [41]. Kumar and Mishra demonstrated, via molecular simulation, the mechanism of solvent-assisted exfoliation to turn bulk MoS_2 into $FLMoS_2$ by applying a shock-wave method [43].

MoS_2 presents several polymorphs, depending on the interlayer stacking arrangement and intralayer coordination between the central Mo atom and the surrounding S atoms, the crystal structures of which are shown in Figure 1 [41,44,45]. The MoS_2 polymorphs are identified using an adapted version of Ramsdell's notation that was introduced for SiC polytypes [46]. This nomenclature indicates the number of S-Mo-S layers in the unit cell (1, 2, or 3) and the crystal system of the lattice, where "T", "H", and "R" stand for trigonal, hexagonal, and rhombohedral, respectively [47]. Five polymorphic forms have been identified for MoS_2: 1T, 1T′, 1H, 2H, and 3R [4,33,44,48–55]. The forms 1T, 2H, and 3R are polytypes because they differ in terms of stacking configuration. The polytypes 2H and 3R occur naturally, while 1T is a metastable structure. The semiconducting 2H phase is naturally more stable and has been extensively investigated for energy-related applications [56,57], transistors [58], photodetectors [59], valleytronics, spintronic devices, and optoelectric devices [58,60,61]. In the 2H-MoS_2 phase, each Mo coordinates with S atoms in a trigonal prismatic arrangement, with two layers in each unit cell in hexagonal symmetry, as shown in Figure 1. The semiconducting behavior of 2H-MoS_2 results from a finite band gap between filled $d_z{}^2$ and empty $d_x{}^2{}_{-y}{}^2{}_{,xy}$ bands [62]. The 2H-MoS_2 phase can easily be turned into the 1T phase by exfoliating the 2H-MoS_2 nanosheets, using the sonication-assisted lithium intercalation method, and treating the resulting material with an infrared laser [63].

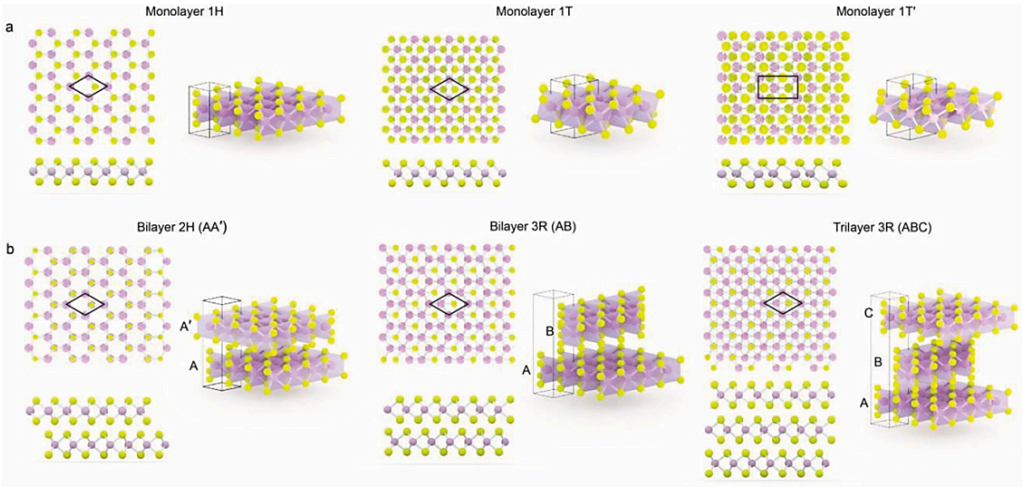

Figure 1. Atomic structures of various polymorphs of MoS_2. (**a**) Monolayer structures; (**b**) bilayer and trilayer structures (yellow—S atoms; purple—Mo atoms). A, A', B and C represent S-Mo-S layers. AA', AB and ABC represent the stacking order sequence Reproduced from [44], with permission from John Wiley & Sons, Copyright 2018 Wiley–VCH GmbH.

With the same prismatic coordination as the 2H MoS_2, but with three stacking layers of S–Mo–S directed along the c-axis instead of two (Figure 1), the rhombohedral 3R phase is also a naturally occurring semiconducting phase. Due to the broken inversion symmetry, this phase has drawn extensive attention because of its potential applications for non-linear optical devices [64–66]. Compared to monolayers, the 3R phase presents a higher predicted piezoelectricity coefficient [64]. The 3R-phase can be synthesized via homoepitaxial growth through chemical vapor deposition [67,68]. Through heating, the 3R phase can easily turn into the 2H phase [69].

The monolayered 1T, 1H and 1T'-MoS_2 phases are other polytypes that have attracted attention but do not occur naturally. Depending on the S-atom's geometry coordination, the Mo atom can be coordinated by six S atoms in either an octahedral (1T) or trigonal prismatic (1H) arrangement [44]. The 1T-phase can be obtained via exfoliation of the 2H-phase [70]. It is metallic in nature, with an electrical conductivity 10^7 times higher than the 2H phase, and is of interest as a supercapacitor electrode material [70,71]. This metastable and paramagnetic phase has been reported to be efficient as a photocatalyst for hydrogen evolution and gas molecule adsorption, due to the high surface activity at the basal sites [44,45,52,53,62,70]. It is also known that the 1T phase can turn into the 2H phase with high-temperature treatment [62]. The semimetallic 1T'-phase, the more stable $SLMoS_2$ with a distorted structure, due to the clusterization of Mo atoms, is formed through the dimerization of Mo atoms in the 1T phase [54]. The 1H phase is a semiconductor. It is possible to turn 1H-MoS_2 into 1T-MoS_2 by applying the Li intercalation method, in which an electron is transferred from the alkali metal to the *d* orbital of the transition metal center, resulting in the metallic-like character of the material [54].

The phase composition influences the photocatalytic performance of MoS_2 nanosheets. Materials comprising 1T/2H phases have shown higher performance in the photodegradation of methyl orange dye, compared to the 2H and 3R phases [69]. Computational studies have indicated that this enhanced photocatalytic activity is due to the emergence of mid-gap states upon the introduction of 1T sites to the 2H lattice. Density functional theory (DFT)-based calculations investigating the material's structural and electronic properties found a zero tunnel-barrier height in stable 2H/1T heterostructures, which is advantageous for achieving an efficient carrier injection rate [72].

Regarding the adsorptive properties, according to the principle of a "hard and soft acid and basis" (HSAB), soft acids (such as heavy metal ions) are capable of strong interaction with soft bases, such as sulfur atoms [73]. Thus, the MoS_2 nanosheets show high adsorption capacity due to the abundance of adsorption sites and the fast kinetics caused by easy

access to those sites [74]. Concerning solubility, MoS_2 is soluble in aqua regia and in hot concentrated sulfuric acid, but it shows insolubility in water and diluted acid, indicating long-term stability in water systems [75].

3. Common Synthesis Methods and Modifications of MoS_2

MoS_2 nanosheets can be synthesized through top-down methods, which consist of exfoliating the bulk MoS_2, and the bottom-up approach, consisting of growing nanosheets from single atoms using chemical methods such as chemical vapor deposition (CVD) or the hydrothermal method. Exfoliation processes are highly efficient and conveniently scalable, producing by-products that are less hazardous and lower costs than bottom-up methods [76,77]. However, bottom-up methods provide better control of phase composition and morphology. Figure 2 shows electron microscopy images illustrating the morphology of MoS_2 obtained by different methods where the difference between top-down methods and bottom-up methods is visible. While the bottom-up methods present defined nanosheets (Figure 2d–f), top-down methods create structures with irregular morphology (Figure 2a–c).

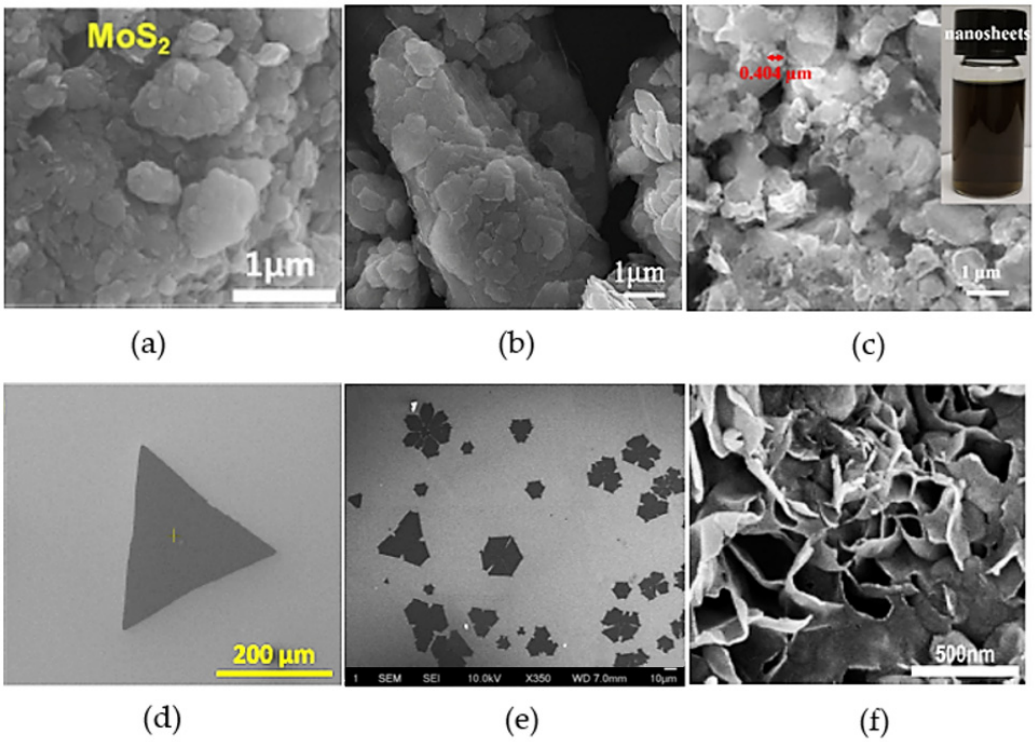

Figure 2. Electron microscopy images of MoS_2, synthesized using different methods: (**a**) Ball-milling method. Reprinted from [78]. Copyright (2018), with permission from Elsevier. (**b**) Ball-milling method. Reprinted from [79]. Copyright (2020), with permission from Elsevier. (**c**) Liquid phase exfoliation method. Reprinted from [80]. Copyright (2019), with permission from Elsevier. (**d**) Chemical vapor deposition method. Reprinted from [81]. Copyright (2021), with permission from Elsevier. (**e**) Chemical vapor deposition method. Adapted from [82]. Copyright (2020), with permission from Elsevier. (**f**) Hydrothermal method. Reprinted from [83]. Copyright (2019), with permission from Elsevier.

3.1. Top-Down Methods

One of the main top-down methods is mechanical exfoliation through the 'Scotch-tape' method. The basis of this method is to strip the MoS_2 flakes using tapes. The 'Scotch-tape' method is considered a non-destructive method in which chemical reactions are not involved [10]. Although this method has a low yield, is time-consuming, and leads to a low quantity of product, it produces $SLMoS_2$ in the form of flakes and is a simple process requiring accessible equipment. This technique also enables MoS_2 with high quality and

crystallinity in 2D [10,84]. Ball-milling is another mechanical exfoliation method. This method can be employed in both dry and wet states. Dry ball-milling can be used to greatly enhance the electrochemical and catalytic properties of bulk MoS_2 [85]. However, wet ball-milling leads to the increased production of $FLMoS_2$ when compared to dry ball-milling [10]. According to Tayyebi et al. [86], the pre-functionalization of the materials can weaken the force interacting between the layers, facilitating exfoliation during the ball-milling process.

Another top-down method is liquid-phase exfoliation. In this approach, the bulk material is dispersed in a solvent and then exfoliated via mechanical processes, such as ultrasonication [87]. This method enables the high-yield creation of 2D flakes in suspension as a scalable production [88,89]. However, after long periods of inactivity or after taking the solvent out, the nanosheets could restack back into bulk form. The addition of a polymer may stabilize the MoS_2 nanosheets, thereby maintaining the properties of exfoliated nanosheets. For instance, Deepak et al. [77] added the polymer poly(vinylidene fluoride-co-hexafluoropropylene) (PVDF-HFP) and used dimethylformamide (DMF) as a solvent in the liquid-phase exfoliation method. Due to its surface energy, water is not considered a suitable solvent for this method. However, hot water has already been employed to exfoliate MoS_2, with satisfactory results [87]. The liquid-phase exfoliation can be assisted by ion intercalation to enhance the yield. Ions such as lithium can penetrate the layers of MoS_2, weakening the interlayer forces and facilitating the detachment of the layers, allowing the production of $SLMoS_2$. However, this method decreases the semiconducting properties of the resulting MoS_2 [37].

3.2. Bottom-Up Methods

The chemical vapor deposition (CVD) method enables a controllable route to decompose Mo and S precursors and assemble them into nanosheets [10]. The MoS_2 nanosheets obtained by CVD are thin, of high quality and high purity, and present limited defects as 2D materials [90]. This method is also indicated for producing $SLMoS_2$ in large quantities at a low cost. However, it presents low control in terms of target products [91] and lacks good reproducibility since it depends on various parameters, such as temperature, pressure, and reaction time, among others [81]. The possibility of forming both $SLMoS_2$ and $FLMoS_2$ zones is also a limitation.

An alternative bottom-up approach that is frequently used is the hydrothermal method. In this method, the MoS_2 crystallizes from aqueous or organic solutions processed at high pressure and temperature [10]. This method achieves high yield, controllable size, and uniform thickness [10]. Although the hydrothermal method is widely used, the mechanism is unclear as the reaction occurs in a closed environment, an autoclave [10]. Different precursors can be used in this method. Khabiri et al. [92] used the hydrothermal method to prepare composites containing MoS_2 nanoflower structures, consisting of adding ammonium molybdate, thiourea, and water to an autoclave and setting the temperature to 180 °C for 20 h. Other authors used a similar procedure, but added ammonium tetrathiomolybdate, ethanol, and water to an autoclave heated at 200 °C for 10 min [93].

In the hydrothermal method, the morphology and properties of MoS_2 can be modified by adjusting the experimental synthesis conditions. Luo et al. [83] observed different morphologies, depending on the S:Mo molar ratio of the starting materials of molybdenum oxide (MoO_3) and potassium thiocyanate (KSCN). Low ratios led to the formation of nano-flower structures (Figure 3a), while at higher ratios (Figure 3b), only nanosheet structures were observed. The temperature and time of the synthesis can also influence the morphology. It was found that at a lower temperature (150 °C) for 25 h, the resulting morphology was like a coral (Figure 3c); when increasing either the time or temperature, the dominant morphology was a flower-like structure (Figure 3d), with size increasing over the synthesis time. At higher temperatures and longer reaction times (240 °C for 47 h), the observed structure consisted of large nanosheets, showing the largest surface area. Other structures, such as core-shell or hollow structures, have been produced, aiming

to enhance the properties of MoS_2 [94,95]. Wu et al. [95] produced 2-μm diameter hollow MoS_2 microspheres via the hydrothermal method and used this material to adsorb the organic contaminant, methyl orange.

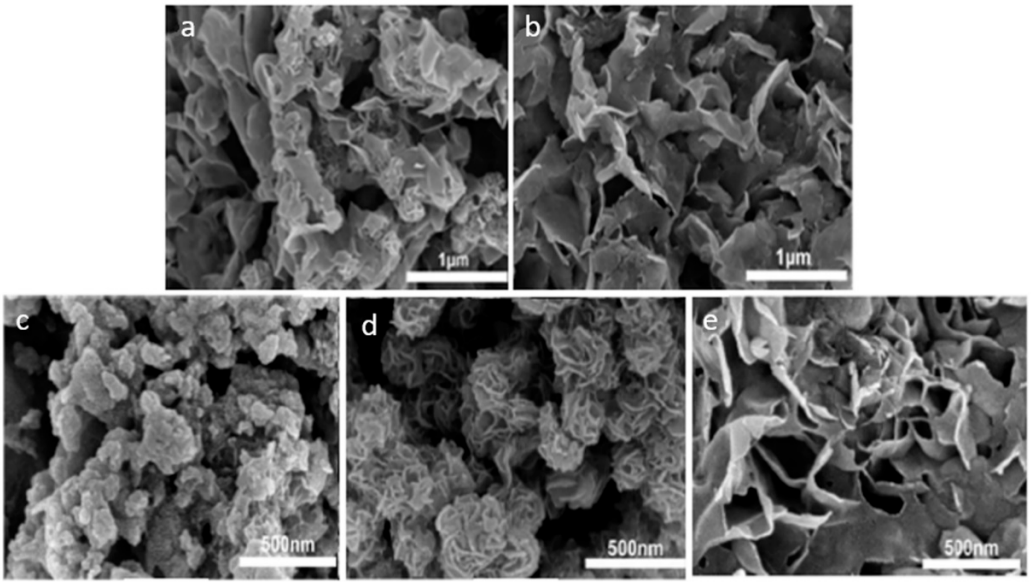

Figure 3. SEM images of MoS_2 composites synthesized via the hydrothermal method. (**a**) S/Mo molar ratio 1:1; (**b**) S/Mo molar ratio 4:1; (**c**) synthesis time: 25 h at 150 °C; (**d**) synthesis time: 37 h at 180 °C; (**e**) synthesis time: 47 h at 240 °C. Reprinted from [83]. Copyright (2019), with permission from Elsevier.

3.3. MoS_2 Modification Methods

The properties of MoS_2 can be modified by expanding the interlaying spacing, a strategy that has been applied in the fields of batteries and photocatalysis [96]. Ai et al. [97] produced a widened defect-rich nano MoS_2 (W-DR-N-MoS_2) via the hydrothermal method to adsorb mercury (Hg^{2+}). The interlayer spacing could be controlled by the synthesis temperatures. The produced MoS_2 consisted of layers of MoS_2 with a wider space between them (d = 9.4 Å against d = 6.15 Å for MoS_2 powder); empty spaces in the layers also characterized this material. Both aspects improved the adsorption capability by enabling adsorption between the layers.

The combination of MoS_2 with other components can lead to materials with improved adsorption capacity. For example, kaolin was used as a substrate for MoS_2 growth via the hydrothermal method. The resulting composite showed increased pore volume, a larger number of adsorption sites, and a consequently greater Pb(II) adsorption efficiency than their counterparts [98]. On the other hand, using montmorillonite (MMT) decreased the hydrophobicity of MoS_2, increasing the dispersibility in water and improving the adsorptive removal of Hg(II) [99]. The growth of Fe_3O_4 nanoparticles onto MoS_2 nanosheets resulted in MoS_2 composites with enhanced conductivity and magnetic behavior [100,101].

Doping MoS_2 with heteroatoms can also modify the MoS_2 properties by regulating the electronic structure and conductivity, regulating the interlaying spacing, and increasing the number of active sites [102–104]. This type of modification has been shown to be effective in photocatalytic hydrogen production and battery fields [102–104]. Doping with metallic elements may lead to undesirable consequences, such as the reduction in stability of MoS_2 by promoting the formation of the MoS_3 phase. In contrast, using non-metallic elements promotes an increased number of active sites and conductivity [103]. Xin et al. [102] synthesized P-doped MoS_2 for photocatalytic hydrogen production. P-doped MoS_2 exhibited broader spectra absorption and a hydrogen production rate 2.8 times higher than the MoS_2 counterpart.

Phase engineering is an approach in which several phases are combined to obtain optimal MoS_2 properties. As mentioned above, a combined 1T/2H phase achieved better results in the photodegradation of methyl orange due to the increased conductivity of the 1T phase and the defects present in this phase [69]. An identical MoS_2 phase combination was used in the photodegradation of potassium hexyl dithiocarbonate, which is an organic pollutant in mine wastewater [105].

An alternative strategy to modify the MoS_2 properties is defect engineering, which consists of creating defect sites in MoS_2 layers to act as active sites for catalysis [69,97]. Luo et al. [106] produced MoS_2 with S defects using a ball-milling method in ascorbic acid, an organic acid-reducing agent. The resulting S defect-rich ultrathin MoS_2 nanosheets were used to photo-reduce Cr(VI). This procedure leads to the formation of two types of S-defects: point defects that may act as recombination centers for photogenerated carriers, and stripping defects that promote the separation of photogenerated electron-hole pairs. According to the authors, combining both types of defects led to an enhancement of photocatalytic performance.

In the normal MoS_2, only the edges sites have active regions with catalytic activity. One way to enhance this property is via the construction of vertically oriented MoS_2 nanosheets (V-MoS_2), which exhibit higher amounts of edge sites, enhanced longitudinal in-plane carrier transport, and stronger light adsorption [107,108]. Liu et al. [107] produced V-MoS_2 by means of CVD induced by a TiO_2 buffer layer, for application in photodetectors. Cui et al. [108] successfully applied a vertical growth MoS_2 construction method in graphene sheets to increase the electrochemical performance of lithium-sulfur batteries.

4. Adsorption Applications

This section reviews the application of MoS_2-based nanomaterials to clean up emerging pollutants from water using adsorptive technologies. Table 1 provides an overview of several MoS_2-based nanomaterials investigated for the adsorption of inorganic and organic contaminants.

Table 1. Kinetics and equilibrium parameters from the fitted models in adsorption studies for the removal of metal ion species and organic contaminants, using MoS_2-based composites.

Composite	MoS_2 Preparation Method	Adsorption Compound	Temperature (°C)	Adsorption Kinetics			Adsorption Isotherms				Ref.
					PFO	PSO	Langmuir		Freundlich		
Metal species											
MoS_2	HT	Hg(II)	27	q_e (mg/g)	208.5	303					[73]
				k_1 (min^{-1})	0.032	-					
				k_2 (g/(mg min))	-	2.710					
				R^2	0.941	0.998					
$Au/Fe_3O_4/MoS_2CAs$	Commercial	Hg(II)		q_e (mg/g)	0.479	20.408	q_m (mg/g)	1527	n	3.040	[109]
				k_1 (min^{-1})	0.089	-	K_L (L/mg)	0.083	K_F (mg/g)	200.85	
				k_2 (g/(mg min))	-	1.2	R^2	0.999	R^2	0.774	
				R^2	0.779	0.999					
3D MoS_2-rGO	HT	Hg(II)	25	q_e (mg/g)		30.55	q_m (mg/g)	400	n	1.046	[110]
				k_1 (min^{-1})	0.117	-	K_L (L/mg)	65.68	K_F (mg/g)	5.936	
				k_2 (g/(mg min))	-	3.75×10^{-3}	R^2	0.9998	R^2	0.999	
				R^2	0.785	0.999					
W-DR-N-MoS_2	HT	Hg(II)		q_e (mg/g)	-	-	q_m (mg/g)	2562.8	n		[97]
				k_1 (min^{-1})	-	-	K_L (L/mg)	3.029	K_F (mg/g)		
				k_2 (g/(mg min))	-	1.42	R^2	0.999	R^2		
				R^2	-	0.9999					
MoS_2/Fe_3O_4	HT	Hg(II)	25	q_e (mg/g)	84.46	254.3	q_m (mg/g)	428.9	N	198.8	[111]
				k_1 (min^{-1})	0.142	-	K_L (L/mg)	1.586	K_F (mg/g)	5.085	
				k_2 (g/(mg min))	-	3.9×10^{-3}	R^2	1.000	R^2	0.723	
				R^2	0.922	1.000					
MoS_2/MMT	HT	Hg(II)	35	q_e (mg/g)	1119.9	1390.81	q_m (mg/g)	2055.9	n	0.759	[99]
				k_1 (min^{-1})	5.426×10^{-3}	-	K_L (L/mg)	0.030	K_F (mg/g)	3.204	
				k_2 (g/(mg min))	-	3.840×10^{-6}	R^2	0.944	R^2	0.838	
				R^2	0.982	0.96089					

Table 1. *Cont.*

Composite	MoS_2 Preparation Method	Adsorption Compound	Temperature (°C)	Adsorption Kinetics			Adsorption Isotherms				Ref.
					PFO	PSO	Langmuir		Freundlich		
Metal species											
MoS_2-clinoptilolite	Commercial	Pb(II)	25	q_e (mg/g)	1.317	50	q_m (mg/g)	3.45	n	2.048	[8]
				k_1 (min^{-1})	6.17×10^{-2}	-	K_L (L/mg)	0.38	K_F (mg/g)	1.527	
				k_2 (g/(mg min))	-	2.0×10^{-2}	R^2	0.964	R^2	0.837	
				R^2	0.723	1.000					
MoS_2/Fe_3O_4	HT	Pb(II)	25	q_e (mg/g)	119.1	199.3	q_m (mg/g)	263.6	n	61.62	[111]
				k_1 (min^{-1})	0.011	-	K_L (L/mg)	0.1468	K_F (mg/g)	3.354	
				k_2 (g/(mg min))	-	1.7×10^{-4}	R^2	1.000	R^2	0.841	
				R^2	0.919	0.922					
MoS_2-kaolin	HT	Pb(II)	25	q_e (mg/g)	12.23	65.94	q_m (mg/g)	280.39	n	5.71	[98]
				k_1 (min^{-1})	−0.086		K_L (L/mg)	2.93	K_F (mg/g)	105.43	
				k_2 (g/(mg min))		0.015	R^2	0.863	R^2	0.790	
				R^2	0.0484	0.9922					
MoS_2/LDC	HT	Cr(IV)	25	q_e (mg/g)	7.65	204.08	q_m (mg/g)	306.85	n	8.333	[112]
				k_1 (min^{-1})	1.4×10^{-2}	-	K_L (L/mg)	0.97	K_F (mg^{1-n} L^n/g)	20.73	
				k_2 (g/(mg min))	-	4×10^{-4}	R^2	0.86	R^2	0.76	
				R^2	0.68	0.999					
2D MoS_2	HT	Ag(I)	25	q_e (mg/g)	392.73	410.24	q_m (mg/g)	813.01	n	3.62	[74]
				k_1 (min^{-1})	0.921	-	K_L (L/mg)	0.12	K_F (mg/g)	206.51	
				k_2 (g/(mg min))	-	3.0×10^{-3}	R^2	0.999	R^2	0.911	
				R^2	0.988	0.997					
chitosan-coated MoS_2 1:2	Precipitation method	Au(III)	30	q_e (mg/g)	1230.84	1338.55	q_m (mg/g)	3434.96	n	807.74	[28]
				k_1 (min^{-1})	0.074	-	K_L (L/mg)	0.043	K_F (mg/g)	3.857	
				k_2 (g/(mg min))	-	6.45×10^{-5}	R^2	0.991	R^2	0.938	
				R^2	0.724	0.901					

Table 1. *Cont.*

Composite	MoS_2 Preparation Method	Adsorption Compound	Temperature (°C)	Adsorption Kinetics			Adsorption Isotherms				Ref.
					PFO	PSO	Langmuir		Freundlich		
Organic Contaminants											
MoS_2	HT	Bisphenol A	25	q_e (mg/g)	28.57	30.25	q_m (mg/g)		n		[83]
				k_1 (min^{-1})	-	-	K_L (L/mg)		K_F (mg/g)		
				k_2 (g/(mg min))	-	-	R^2		R^2		
				R^2	0.901	0.998					
rGO/MoS_2	HT	Ofloxacin		q_e (mg/g)	-	43.104	q_m (mg/g)	37.31	n	3.84	[7]
				k_1 (min^{-1})	-	-	K_L (L/mg)	0.46	K_F (mg/g)	15.07	
				k_2 (g/(mg min))	-	2.69×10^{-4}	R^2	0.989	R^2	0.845	
				R^2	-	0.918					
UiO−66/MoS_2	HT	Lomefloxanin		q_e (mg/g)	45.6	80.67	q_m (mg/g)	32.36	n	5.152	[113]
				k_1 (min^{-1})	0.2434	-	K_L (L/mg)	0.28606	K_F ($mg/(g(L/mg)^{1/n})$)	14.957	
				k_2 (g/(mg min))	-	1.7×10^{-4}	R^2	0.786	R^2	0.940	
				R^2	0.974	0.973					
MoS_2/MTT	HT	Atenolol	25	q_e (mg/g)	88.85	96.62	q_m (mg/g)	145.6	n	3.363	[114]
				k_1 (min^{-1})	0.151	-	K_L (L/mg)	0.197	K_F (L/g)	41.38	
				k_2 (g/(mg min))	-	2.364×10^{-3}	R^2	0.974	R^2	0.859	
				R^2	0.957	0.991					
MoS_2/MTT	HT	Acebutolol	25	q_e (mg/g)	63.85	69.25	q_m (mg/g)	130.8	n	2.772	[114]
				k_1 (min^{-1})	0.287	-	K_L (L/mg)	0.107	K_F (L/g)	25.42	
				k_2 (g/(mg min))	-	5.617×10^{-3}	R^2	0.945	R^2	0.831	
				R^2	0.829	0.982					

Table 1. *Cont.*

Composite	MoS_2 Preparation Method	Adsorption Compound	Temperature (°C)	Adsorption Kinetics			Adsorption Isotherms				Ref.
					PFO	PSO	Langmuir		Freundlich		
Organic Contaminants											
h-MoS_2	HT	MO	25	q_e (mg/g)	12.86	42.44	q_m (mg/g)	38.11	n	1.897	[91]
				k_1 (min^{-1})	0.518	-	K_L (L/mg)	0.285	K_F ($mg/(g(L/mg)^{1/n})$)	5.342	
				k_2 (g/(mg min))	-	9.35×10^{-3}	R^2	0.952	R^2	0.992	
				R^2	0.848	0.999					

h-MoS_2—hollow MoS_2 microspheres; HT—hydrothermal method; k_1—rate constant of pseudo-first-order kinetic model; k_2—rate constant of pseudo-second-order kinetic model; K_F–Freundlich constant; K_L—Langmuir constant; LDC—lignin-derived carbon; MMT—montmorillonite; MO–methyl orange; MoS_2CAs—MoS_2 composite aerogel; n–heterogeneity factor; PFO—pseudo-first-order kinetic model; PSO—pseudo-second-order kinetic model; q_e—adsorption capacity at equilibrium; q_m—maximum adsorption capacity; rGO—reduced graphene oxide; W-DR-N- MoS_2—widened defect-rich nano MoS_2.

4.1. Heavy Metal Species

Pollution with heavy metal species is a huge concern because it represents a high risk for the environment and for humans [8]. Heavy metal ions are toxic, non-biodegradable, persistent in the environment, and tend to accumulate in organisms, causing health issues [8]. Lead (Pb(II)) is one of the most common ions found in industrial wastewater and shows toxicity, even at low concentrations ($\geq$15 µg/L in drinking water) [8]. Many problems, such as anemia, hypertension, reduced intelligence quotient, and immunotoxicity are related to Pb(II) exposure [8]. Mercury is another heavy metal that presents a high risk to human health and may cause kidney failure, severe pulmonary irritation, neurological disorders, and death [73]. Mercury exists in the form of several inorganic (e.g., metallic mercury or mercuric salts (Hg(II)) and organometallic species (e.g., methylmercury). The Hg(II) species can also affect the food chain once they can bioaccumulate [73]. Chromium, particularly chromium (VI), is hazardous to human health as well [112]. In this oxidation state, Cr(VI) can cause cancer and fetal malformations with only a concentration higher than 0.10 mg/L in drinking water [112].

As stated above, MoS_2 has good adsorption capability for heavy metal ions due to the sulfur atoms on the surface. For this reason, MoS_2 has been investigated in terms of the adsorptive removal of these pollutants from water. Table 1 lists the most relevant studies. Most of the studies focused firstly on Hg(II) removal, due to its high toxicity, and, secondly, on Pb(II) and Cr(VI) removal. For instance, Pirarath et al. [73] produced nanosheets of MoS_2 via surfactant-assisted hydrothermal synthesis, using sodium dodecyl sulfate (SDS), and investigated the adsorption of Hg(II) in batch conditions. The negative charge of the S layers increased with SDS, which induced an electrostatic interaction between Hg(II) and MoS_2. A higher adsorption capacity was achieved due to the excess negative charge of the S layer, compared to the nanosheets of MoS_2 produced by other methods. Within 300 min, 0.5 g/L of the composite enabled 93% removal of Hg(II) in distilled water samples. Ai et al. [97] produced a widened defect-rich nano MoS_2 (W-DR-N- MoS_2), with many sulfur binding sites exposed due to enlarged interlayer spacing. With this modification, Hg(II) removal of 99.8% was achieved in just 5 min in distilled water samples, using 0.1 g/L of the material. The Hg(II) removal was also efficient in both natural water and industrial wastewater samples. The recovery of the adsorbent is economically important. Coupling a magnetic component to MoS_2 has been investigated as a strategy to facilitate its separation; employing a magnetic field is an accessible method. Zhi et al. [109] produced an aerogel of MoS_2 and GO with embedded Fe_3O_4 and Au NPs ($Au/Fe_3O_4/MoS_2CAs$) to remove Hg(II). A removal performance of 100% was achieved in only 30 min with 0.5 g/L of $Au/Fe_3O_4/MoS_2CAs$, which is a great achievement for Hg(II) adsorption. The reuse of this composite for up to 10 cycles only slightly decreased the efficiency of the adsorption. Wang et al. [111] used flower-like MoS_2 decorated with Fe_3O_4 to investigate the simultaneous removal of Hg(II) and Pb(II) from distilled water, along with Pb(II) removal in real battery wastewater and soil samples, achieving satisfactory results. Yuan et al. [98] produced a MoS_2-kaolin composite for Pb(II) adsorption, reaching a 99.9% removal rate in 40 min with 1.6 g/L of composite. According to the authors, using kaolin induces uniform MoS_2 growth and a higher pore volume, leading to more adsorption sites. Regarding the Cr(VI) removal, Chen et al. [112] produced MoS_2/lignin-derived carbon (MoS_2/LDC) and achieved 99.4% removal of Cr(VI) in distilled water samples after 30 min, using just 0.10 g/L of composite.

It is essential to evaluate the selectivity of the adsorbents toward the target pollutant because in natural water or wastewater, there are other species that can compete for sorption sites. In this context, Zhi et al. [109] evaluated the selectivity of the magnetic $Au/Fe_3O_4/MoS_2CAs$ composites toward Hg(II) capture via a mixture of a large number of ions in a synthetic water sample. Despite the presence of several ions (Na(I), K(I), Ag(I), Ca(II), Ba(II), Mg(II), Fe(II), Cu(II), Zn(II), Ni(II), Cd(II), Al(III), Pb(II), Cr(III) and Hg(II)) the most adsorbed ion was Hg(II). All the other ions did not show relevant adsorption.

The reason for this selectivity may be related to the HSAB principle, i.e., soft acids such as Hg(II) establish strong interactions with soft bases such as sulfur [111,115].

After adsorption tests, the composite with the adsorbed heavy metal ion can be separated from the solution and treated, aiming for a reduction in the heavy metal ions, which precipitate and desorb from the catalyst [111,112].

Besides the heavy metal species, MoS_2-based materials have been employed for the capture of noble metal species, namely, silver and gold ions. The recovery of these metals from industrial effluents and wastewater is important, not only to prevent pollution but also because of their economic value [28,74]. Zeng et al. [74] produced a 2D MoS_2 to remove Ag(I) from distilled water samples. The mechanism of adsorption was investigated using X-ray photoelectron spectroscopy (XPS) and DFT calculations, confirming a strong interaction between MoS_2 and Ag(I) by the complexation of Ag-S and Ag-O through hybridization between the d orbital of Ag and the p orbital of S or O [74]. The recovery of gold ions (Au(III)) has also been investigated [28]. Using chitosan-coated MoS_2 (0.28 g/L dose), Zhao et al. [28] achieved 98.9% ion removal in 300 min. The ion-selectivity of chitosan-coated MoS_2 in wastewater containing Au(III), Cu(II), Mg(II), Ni(I), Li(I), and Zn(II) species was evaluated. It was found that the biosorbent presented the highest selectivity to the Au(III) ions and the lowest affinity to Zn(II) ions. After adsorption, desorption enabled the recovery of noble metal ions for further use.

4.2. Organic Contaminants

The adsorption of organic contaminants using MoS_2-based materials was less widely investigated. MoS_2-based membranes for organic contaminant removal are beyond the scope of this work and have recently been reviewed elsewhere [13]. Most research papers that present results of the adsorption of organic contaminants have, as their primary focus, the study of the photodegradation of these contaminants. Table 1 lists several studies of the adsorption of organic contaminants. MoS_2 nanosheets produced by the hydrothermal method removed nearly 82.3% of Bisphenol A (BA), which is an endocrine disruptor, after 120 min with a sorbent dosage of 1.5 g/L [83]. Reduced graphene oxide-MoS_2 (rGO-MoS_2) composites successfully removed the ofloxacin antibiotic [7]. Despite the low surface area (17 m^2/g), 95% removal was achieved after 240 min with 0.35 g/L of adsorbent. The adsorption capacity in real wastewater samples was also investigated. However, the removal drastically decreased after composite reuse, and only 4% was removed after 10 cycles. Gao et al. [113] produced a composite with a metal–organic framework (UiO-66/MoS_2) and report a comprehensive study on the adsorption and photocatalytic degradation of lomefloxacin. The beta-blockers, atenolol and acebutolol, were also adsorbed successfully in distilled water with MoS_2/montmorillonite (MoS_2/MTT) composites [114]. Regarding the adsorption of dyes, methyl orange was adsorbed by hollow MoS_2 microspheres (h-MoS_2) [95]. The adsorption equilibrium was achieved in just 10 s for MO, with a maximum adsorption capacity of 42 mg/g.

MoS_2-based composites have also been used for the adsorption of various organic dyes. Song et al. [100] produced MoS_2 decorated with Fe_3O_4 nanoparticles and tested this composite for the adsorption of Congo red (CR), methylene blue (MB), methylene green (MG), rhodamine B (RhB) and eosin Y (EY). Among these dyes, the composite showed higher adsorption of CR with an adsorption capacity of 71 mg/g, achieving the removal of about 65.2% in 2 min, which increased to 71% after 120 min with 1 g/L of the composite.

4.3. Kinetic and Isotherm Studies

Table 1 presents a summary of relevant information on the kinetics and equilibrium adsorption tests employing MoS_2-based materials. Overall, the kinetic model that better described the results was the pseudo-second-order (PSO) kinetic model, with an R^2 value of between 0.901–1.000, indicating a good fit of this model to the adsorption data of both the metal species and organic contaminants. Regarding the equilibrium description, the Langmuir model better described the adsorption data (R^2 = 0.86–1.0). However, the equi-

librium adsorption of the antibiotic lomefloxacin and MO dye was better described by the Freundlich isotherm model, indicating non-monolayer formation [83,115]. Wang et al. [111] used flower-like MoS_2 decorated with Fe_3O_4 nanoparticles in the removal of Hg(II) and Pb(II) from an aqueous environment. The maximum adsorption capacity estimated by the Langmuir model was 428.9 mg/g for Hg(II) and 263.6 mg/g for Pb(II), under optimized conditions (pH 5, 25 °C, 0.8 g L^{-1} sorbent dosage). The adsorption kinetics were well described by the PSO model and the good fitting of the Langmuir isotherm model was in line with monolayer formation. The favorable adsorption capacity, selectivity, and recyclability originated from the strong interaction between S and the heavy metal ions. The MoS_2-clinoptilolite composite removed nearly 100% (99.8%) of Pb(II) from aqueous solution (pH 6, 25 °C, starting concentration of 50 mg L^{-1}, 1.5 g L^{-1} sorbent dosage) after 90 min [8]. This adsorption was ascribed to the interaction of Pb(II), not only with the S layers of the MoS_2 but also with the -OH and -COOH functional groups of clinoptilodite. The thermodynamic parameters were calculated and indicated that the adsorption was spontaneous and exothermic in nature.

Looking at the equilibrium adsorption values (*qe*) of the metal species in Table 1, the highest value found was 3435 mg/g (R^2 = 0.991) for the adsorption of Au(III) at an optimal pH of 5, using chitosan-coated MoS_2 (CS/MoS_2) crosslinked with glutaraldehyde. The value was estimated by the Langmuir model and was close to the experimental value (3109 mg/g) [28]. The adsorption capacity increased and the adsorption isotherm changed from multilayer to monolayer when the content of MoS_2 increased. The highest adsorption capacity was observed for a mass ratio of 1:2 (CS:MoS_2), at 35 °C, after 300 min. The high efficiency of these materials to adsorb Au(III) was ascribed to electrostatic interaction, in the form of tetrachloroaurate ions ($AuCl_4^-$) and then to complexation by the sulfur- and nitrogen-containing functional group. The materials also showed outstanding selectivity for gold ions in the presence of coexisting ions and demonstrated attractive reusability after four cycles.

Concerning the organic contaminants, the highest adsorption capacity was observed for atenolol, using MoS_2/MTT as an adsorbent (*qe* = 146 mg/g) and close to the value estimated by the Langmuir model (132 mg/g) [114]. The adsorption kinetics could be described using the PSO model. The interactions leading to the adsorption included van der Waals interactions and hydrogen bonding between the hydroxyl groups of the atenolol and the sorbent. The quantum chemical calculations results were in line with the lower adsorption capacity observed for acetobutolol using the same adsorbent.

Other parameters and isotherm models have been used to characterize the adsorption, such as the distribution coefficient, which expresses the affinity of a compound to the adsorbent, and Temkin isotherm, which assumes that the heat of adsorption does not remain constant during the adsorption process [74,110].

5. Photocatalytic Applications

Adsorption is an excellent approach to removing pollutants from wastewater. However, this technique does not provide a complete solution to the problem since the contaminants are not mineralized. In this sense, advanced oxidation processes (AOPs), such as photocatalytic oxidation, have been developed to promote the degradation of pollutants [116].

Due to the relatively small band gap of MoS_2, visible-light irradiation can induce a catalytic chain reaction. For bulk MoS_2, the band gap is ~1.2 eV, which means that MoS_2 is activated with almost all the solar spectrum, while SLMoS_2 shows a band gap of ~1.8 eV, this phase being activated by a radiation wavelength of <660 nm. However, as the bulk MoS_2 has unsaturated Mo and S atoms at the edge, leading to an indirect and small band gap, this is insufficient to achieve photocatalytic reactions. For this reason, bulk MoS_2 is not suitable for photocatalysis [117].

MoS_2 has been combined with several components to improve its performance as a photocatalyst to degrade contaminants. Table 2 lists several recent studies on the photo-

catalytic degradation of pollutants in water. MoS_2-based materials have been primarily employed in the photodegradation of dyes. Dye-related industries are reported as the major source of contaminated wastewater [118]. Dye-containing wastewater presents both chromaticity and toxicity [25,119]. Pharmaceuticals, antibiotics, and pesticides, among other chemical compounds, also represent emerging contaminants where photodegradation has been investigated, due to their toxicity and increasing detection in wastewater [119]. The same photocatalyst could photodegrade various contaminants at different rates. For example, Fu et al. [120] reported degradation rates above 70% for methylene blue (MB), methyl orange (MO), and Congo red (CR), using ZnO/MoS_2 nanoarrays. In contrast, the degradation of rhodamine B (RhB) dye was only around 8%. Regarding the degradation of MB, Khabiri et al. [92] achieved 83% degradation after 1 min of irradiation with VIS light, that increased to 91% after 120 min using α-Fe_2O_3/MoS_2 QDs, a composite comprising hematite (α-Fe_2O_3) and nanosized MoS_2 (MoS_2 quantum dots (QDs)). Figure 4 illustrates the proposed photocatalytic mechanism. The visible light irradiation excites the electrons (e^-) in the valence bands (VB) of α-Fe_2O_3 and MoS_2QDs to the respective conduction bands (CB), leaving a hole (h^+) in the VB. The CB and VB positions of MoS_2QDs are above α-Fe_2O_3. Due to the potential energy difference, the photogenerated electrons at the CB of MoS_2QDs transfer to the CB of α-Fe_2O_3, then migrate to the surface of the catalyst, which enables the creation of the reactive species as a superoxide anion radical ($\cdot O_2^-$) by the reaction with O_2, and hydroxyl radicals ($\cdot$OH) from reaction with water. The reactive species react with MB, thereby degrading it [92]. Most of the values for the degradation rate presented in Table 2 are above 70% for different contaminants, MoS_2-based catalysts, and methodologies. For MB, the highest degradation rate was 97%, after 40 min of reaction using 1 g/L of MZO (MoS_2/ZnO) [121]. A similar degradation rate was obtained in just 5 min using the ternary catalyst MoS_2/$BiFeO_3$/Ag_3PO_4 under ultraviolet-visible (UV-Vis) irradiation [119]. The same catalyst achieved a good degradation of MO and RhB, with 98% and 97% degradation, respectively, after 5 min of irradiation (Table 2) [119]. Regarding other contaminants from the antibiotic spectrum, tetracycline (20 mg/L) was successfully degraded up to 99% within 50 min under visible light, catalyzed with 0.4 g/L MoS_2/Eu/B-g-C_3N_4 (MoS_2/BEuCN) as the catalyst [122]. Ahamad et al. [123] studied the photocatalytic degradation of bisphenol-A (BA) using the composite g-C_3N_4/MoS_2−PANI, achieving 93% of removal after 60 min under visible light. DFT calculations were performed to elucidate the photocatalytic degradation mechanism of BA. It was proposed that the aromatic ring would be one of the most likely sites for an attack by photo-generated radicals, which leads to several intermediate species and to the production of the final products, CO_2 and H_2O [123].

Table 2. Characteristics of MoS_2-based catalysts and the respective photocatalytic performance (in optimized conditions).

MoS_2-Based Catalyst	Contaminant	MoS_2 Production Method	Band Gap (eV)	CSA (m^2/g)	Irradiation	Irradiation Time (min)	Removal Rate	PFO Kinetics k (min^{-1})	Ref.
Dyes									
α-Fe_2O_3/MoS_2QDs	MB	HT	2.22	5.852	Vis (400–700 nm)	1 120	83% 91%	1st min 0.892 > 28 min 0.0049	[92]
MoS_2/ZnO	MB	HT	-	14.785	Vis	40	97%	0.0701	[121]
5 wt% MoS_2/$BiFeO_3$/Ag_3PO_4	MB	C	2.07	7.705	UV-Vis	5	97%	0.625	[119]
ZnO/MoS_2 8 h	MB	LPE	1.77	-	UV-Vis	37.5	Vis-85% UV-78%	-	[124]
Ni foam with ZnO/MoS_2	MB	HT	-	4.85	UV-Vis	50	72%	-	[120]
1.9% MoS_2/g-C_3N_4/PAN	MB	HT	2.76	15.6	Vis (>420 nm)	120	85%	-	[125]
MoS_2/Fe_3O_4 (MF-17)	MB	HT	-	4,5	Vis	120	98%	-	[25]
CM12 (Cu_2O/MoS_2)	MB	HT	Cu_2O—2.15 MoS_2—1.76	-	Vis (>420 nm)	30	90%	0.084	[126]
MoS_2-TiO_2	MO	HT	2.76	103.5	-	60	86%	0.016	[127]
CoO/meso-CN/MoS_2 (1%) (S6)	MO	HT	2.82–2.86	37.64	VIS	60	84%	-	[118]
5 wt% MoS_2/$BiFeO_3$/Ag_3PO_4	MO	C	2.07	7.704	UV-Vis	5	98%	0.376	[119]
g-C_3N_4/MoS_2/TiO_2 (CMT5)	MO	HT	2.64	97.5	Vis (400–700 nm)	60	98%	0.061	[128]
Ni foam with ZnO/MoS_2	MO	HT	-	4.85	UV-vis	10	93%	0.059	[122]
5% MoS_2/ZnO	RhB	HT	3.18	-	UV	50	95%	0.057	[119]
5 wt% MoS_2/$BiFeO_3$/Ag_3PO_4	RhB	C	2.07	7.704	UV-Vis	5	97%	0.676	[119]
Ag/MoS_2/CC	RhB	HT	-	27	Vis	20 40	90% 99%	72.1×10^{-3}	[129]
CTAB-MoS_2-P25	RhB	HT	2.06	-	-	120	91%	-	[130]
Ni foam with ZnO/MoS_2	RhB	HT	-	4.85	UV-vis	80	8%	-	[120]
1.9% MoS_2/g-C_3N_4/PAN	RhB	HT	2.76	15.6	Vis (>420 nm)	120	48%	0.006	[125]

Table 2. *Cont.*

MoS_2-Based Catalyst	Contaminant	MoS_2 Production Method	Band Gap (eV)	CSA (m^2/g)	Irradiation	Irradiation Time (min)	Removal Rate	PFO Kinetics k (min^{-1})	Ref.
Dyes									
$BiOI/MoS_2$ (BMS-8)	RhB	HT	BiOI—1.42 MoS_2—1.73	30.76	Vis (>420 nm)	90	100%	0.023	[3]
MoS_2/Fe_3O_4 (MF-17)	RhB	HT	-	4,5	Vis	120	96%	-	[25]
g-C_3N_4/MoS_2/GO (AT3G15)	RhB	HT	2.05	-	Vis	60	99%	-	[131]
5wt% $MoS_2/BiFeO_3/Ag_3PO_4$	Acrid red 18	C	2.07	7.7045	UV-Vis	7	98%	0.484	[119]
CoO/meso-CN/MoS_2(1%) (S6)	Methyl red	HT	2.82–2.86	37.64	Vis	60	96%	0.072	[118]
CoO/meso-CN/MoS_2(1%) (S6)	Congo red	HT	2.82–2.86	37.64	Vis	60	95%	-	[118]
g-$C_3N_4/MoS_2/TiO_2$ (CMT5)	4-Nitrophenol	HT	2.64	97.5	Vis (400–700 nm))	60	87%	-	[128]
MoS_2-ZnS	Crystal violet	HT	-	-	Vis	40	99%	41.26×10^{-3}	[132]
Ni foam with ZnO/MoS_2	Congo red	HT	-	4.85	UV-Vis	80	77%		[120]
MoS_2/g-C_3N_4/TiO_2	Malachite green	HT	2.42	-	Vis	60	86%	0.045	[133]
Antibiotics									
MoS_2/BiOBr/CF	TC	HT	MoS_2_1.81 BiOBr—2.88	-	Vis	120	89%	-	[134]
$Fe_3O_4/MoS_2/BiVO_4$ (FMB3)	TC	HT	MoS_2—1.56 $BiVO_4$—2.44	-	Vis (>420 nm)	120	86%	0.01576	[135]
5 wt% $MoS_2/BiFeO_3/Ag_3PO_4$	TC	C	2.07	7.704	UV-Vis	120	90%	-	[119]
MoS_2/Z-50	TC	HT	-	17.32	Vis (>420 nm)	120	97%	-	[136]
20 wt% MoS_2/BEuCN	TC	HT	2.85	44.12	Vis	50	99%	0.087	[122]
MoS_2/TiO_2/graphene (MTG-48)	TC	HT	3.17	58.6	UV-Vis (300–750 nm)	60	92%	0.05	[137]
MoS_2/ZnO QDs	TC	HT	-	-	Vis	80	96%	0.01	[138]
CdS/MoS_2/ZnO(CMZ)	Ofloxacin	chemical co-precipitation method	CdS—2.145 MoS_2—2.015 ZnO—2.981	-	Vis (>420 nm)	90	89%	0.024	[139]

Table 2. *Cont.*

MoS_2-Based Catalyst	Contaminant	MoS_2 Production Method	Band Gap (eV)	CSA (m^2/g)	Irradiation	Irradiation Time (min)	Removal Rate	PFO Kinetics k (min^{-1})	Ref.
Antibiotics									
UiO-66/MoS_2 (UMS-0.15)	Lomefloxacin	HT	-	37.176	Vis	90	87%	-	[113]
Other organic compounds									
MXene-Ti_3C_2/MoS_2 (MT-4)	Ranitidine	HT	1.59	11.93	Vis	60	88%	-	[140]
rGO10%/ZnO20%/MoS_2	Aniline	HT	2.24	-	Vis	120	100%	-	[141]
MoS_2-TiO_2	4-Nitrophenol	HT	2.76	103.5	Vis	60	97%	0.024	[127]
MoS_2/CuO-25%	2-MBT	HT	MoS_2—1.52 CuO—2.16	47	Vis	120	96%	-	[142]
Cu_2S-1.0%MoS_2	Phenol	C	1.42	-	Vis	90	90%	-	[143]
g-C_3N_4/MoS_2/GO (AT3G15)	4-CP	HT	2.05	-	Vis	60	89%	-	[131]
5 wt% MoS_2/$BiFeO_3$/Ag_3PO_4	2,4-D	C	2.07	7.704	UV-Vis	180	90%	-	[119]
5 wt% MoS_2/$BiFeO_3$/Ag_3PO_4	Acephate	C	2.07	7.704	UV-Vis	60	85%	-	[119]
g-C_3N_4/MoS_2−PANI	Bisphenol-A	HT	2.67	184.21	Vis	60	93%	0.040	[123]
Metal ion species									
MoS_2/BiOBr/CF	Cr(VI)	HT	MoS_2—1.81 BiOBr—2.88	-	Vis	120	85%	-	[134]
Ni foam with ZnO/MoS_2	Cr(VI)	HT	-	4.85	UV-Vis	25	75%	-	[120]
MoS_2/TiO_2/graphene (MTG-48)	Pb(II)	HT	3.17	58.6	UV-Vis (300–750 nm)	60	88%	-	[137]

Note: 2,4-D—2,4-dichlorophenoxyacetic acid; 2-MBT—2-mercaptobenzothiazole; 4-CP—4-chlorophenol; C—commercial; CC—carbon cloth; CF—carbon fiber; CTAB- cetyltrimethyl ammonium bromide; CSA—catalyst-specific area; HT—hydrothermal method; LPE—liquid-phase exfoliation method; MB—methylene blue; MO—methyl orange; PAN—polyacrylonitrile; PANI—polyaniline; PFO—pseudo-first order; QDs—quantum dots; RhB—rhodamine B; Z-50—zeolite; TC—tetracycline.

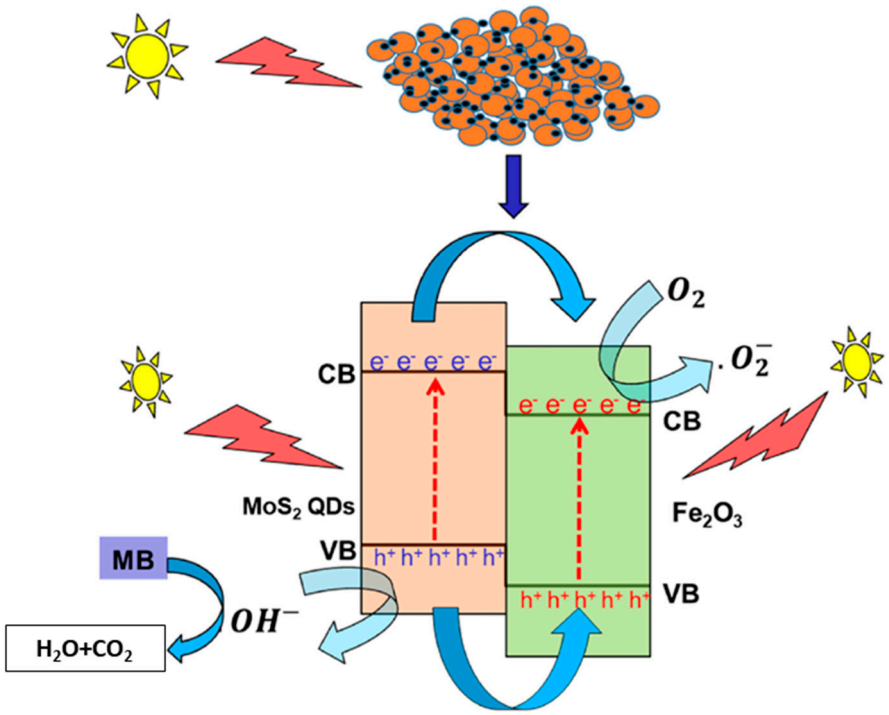

Figure 4. Schematics of the proposed photocatalysis mechanism of α-Fe_2O_3/MoS_2QDs. Reproduced from [92], with permission from John Wiley & Sons. Copyright 2018 Wiley-VCH GmbH.

Although most photodegradation studies rely on organic contaminants, MoS_2-based photocatalysts were also employed to reduce Cr(VI) to Cr(III) [120,134]. As mentioned before, Cr(VI) is a highly toxic form of chromium. By reducing it to Cr(III), the toxicity decreases, and the chromium can be precipitated and removed [144]. Via photo-reduction, 85% Cr(VI) removal was achieved using MoS_2/BiOBr/CF under visible light after 2 h, and 75% Cr removal rate using Ni foam with ZnO/MoS_2 after 25 min under UV-VIS light [120,134]. Shi et al. [134] tested the effect of pH in this photocatalytic reaction and observed the highest removal (91%) at pH = 3 and the lowest removal (29%) at pH = 11. This behavior was ascribed to different chromium speciation according to pH. At pH < 7, the predominant species is the dichromate anion ($Cr_2O_7^{2-}$), which is more likely to be reduced to Cr(III) than the chromate anion (CrO_4^{2-}), which predominates at pH > 7. In addition, using MoS_2/TiO_2/graphene, Chen et al. [137] achieved an 88% removal of Pb(II) in an aqueous solution in just 60 min under UV-Vis light. The removal was higher in an acidic environment (pH < 7) because the dominant species at those pH values ($Pb^{2+}(H_2O)_6$) is more reactive than the other Pb(II) species, due to the more positive charge and smaller hydration radius.

In photocatalysis, the goal is to achieve the total mineralization of the pollutants. This means fully converting the contaminants to a gaseous form, water, salts, and minerals [145]. However, several photodegradation reactions may lead to toxic intermediate compounds, which can harm the environment [146]. The total organic carbon (TOC) quantification method can be employed to evaluate the mineralization of a contaminant achieved by photocatalysis. Table 3 shows a relatively high mineralization rate, with more than 54% of the mineralization provided by MoS_2-based photocatalysts. This means that most of the contaminant molecules present in the solution (>50%) were fully degraded, while part may still be the original contaminant (when the removal rate is less than 100%) or is converted into some intermediate compound. For example, 100% degradation of Rhodamine B was achieved with the BiOI/MoS_2 (BMS-8) catalyst. However, only 78% of the initial amount of the dye was fully mineralized, leaving 23% in the form of intermediate compounds [3]. Overall, the results show the promising potential of MoS_2-based catalysts to photodegrade and mineralize the organic contaminants in wastewater systems.

Table 3. Photodegradation rate and mineralization evaluation on photocatalytic studies, with MoS_2-based catalysts.

MoS_2-Based Catalyst	Contaminant	Irradiation Time (min)	Photodegradation/ Removal Rate	Mineralization Evaluation	Ref.
5 wt % $MoS_2/BiFeO_3/Ag_3PO_4$	MB	5	97%	>85%	[119]
$CoO/meso\text{-}CN/MoS_2$(1%) (S6)	MO	60	84%	54%	[118]
5 wt % $MoS_2/BiFeO_3/Ag_3PO_4$	MO	5	98%	> 85%	[119]
g-$C_3N_4/MoS_2/TiO_2$ (CMT5)	MO	60	98%	91%	[128]
5 wt % $MoS_2/BiFeO_3/Ag_3PO_4$	RhB	5	97%	>85%	[119]
$BiOI/MoS_2$ (BMS-8)	RhB	90	100%	78% *	[3]
g-C_3N_4/MoS_2/GO (AT3G15)	RhB	60	99%	85%	[131]
5 wt % $MoS_2/BiFeO_3/Ag_3PO_4$	Acrid red 18	7	98%	>85%	[119]
$CoO/meso\text{-}CN/MoS_2$(1%) (S6)	Methyl red	60	96%	80%	[118]
$CoO/meso\text{-}CN/MoS_2$(1%) (S6)	Congo red	60	95%	71%	[118]
MoS2/BiOBr/CF	TC	120	92%	55% **	[134]
5 wt % $MoS_2/BiFeO_3/Ag_3PO_4$	TC	120	90%	91%	[119]
MoS_2/TiO_2/graphene (MTG-48)	TC	60	92%	33.8%	[137]
MXene-Ti_3C_2/MoS_2 (MT-4)	Ranitidine	60	88%	74%	[140]
5 wt % $MoS_2/BiFeO_3/Ag_3PO_4$	2,4-D	180	90%	87%	[119]
5 wt % $MoS_2/BiFeO_3/Ag_3PO_4$	Acephate	60	85%	93%	[119]

Note: 2,4-D—2,4-dichlorophenoxyacetic acid; CF—carbon fiber; MB—methylene blue; MO—methyl orange; RhB—rhodamine B; TC—tetracycline; * TOC after 60 min of irradiation; ** TOC after 7 h of irradiation.

6. MoS_2-Based Nanocomposites

Although nano-MoS_2 shows good efficiency as a photocatalyst for removing several contaminants, it can be enhanced when in combination with other components in the form of nanocomposites. Table 4 lists several works comparing the photodegradation provided by bare nano-MoS_2 and MoS_2-based nanocomposites. Overall, MoS_2-based nanocomposites present a higher specific area when compared to bare nano-MoS_2. The increase in the specific surface area of the catalyst can contribute to an enhanced removal rate once a higher exposed specific area favors the contaminant-catalyst contact [142].

Overall MoS_2-based composites presented better adsorptive performance than bare MoS_2. The creation of defects and increasing interlayer spacing were used to enhance the adsorption capacity of Hg(II) from 36 mg/g to 2563 mg/g [97]. The introduction of montmorillonite (MMT) enhanced the water dispersibility of MoS_2 by decreasing the hydrophobicity, which improved the adsorption capacity [99]. For instance, MoS_2/MMT composites adsorbed nearly 1120 mg/g of Hg(II), which is markedly higher than the value observed for bare MoS_2 (937 mg/g). MoS_2/MMT composite was also used to adsorb the beta-blockers atenolol and acebutolol, achieving good results [114]. Kaolin has been used as a substrate, providing a uniform growth of MoS_2 and well-distributed active sites, which improved the removal of Pb(II) from 55% in bare MoS_2 to 89% in MoS_2-kaolin [98].

Table 4. Adsorption and photocatalytic performance of MoS_2-based nanocomposites and a comparison with bare MoS_2.

Adsorption									
Composite	**Contaminant**	**Specific Area (m^2/g)**	**Contact Time (min)**	**Comparative Adsorption Parameters**					**Ref.**
W-DR-N-MoS_2	Hg(II)	-	-	Interlaying spacing	9.42 Å	Maximum adsorption capacity (q_{max}) (mg g^{-1})	2562.8		[97]
MoS_2	Hg(II)	-	-		6.15 Å		35.5		
MoS_2/MTT	Hg(II)	-	-	Adsorption capacity in equilibrium, according to the pseudo-first-order kinetic model (mg g^{-1})			1119.94		[99]
MoS_2	Hg(II)	-	-				936.62		
MoS_2-kaolin	Pb(II)	14.56	10	Adsorption capacity (mg g^{-1})	55.10	Removal rate	89%		[98]
MoS_2	Pb(II)	13.08	10		35.68		54%		
MoS_2/MTT	Atenolol	-	150	Adsorption capacity (mg g^{-1})			132.08		[114]
MoS_2	Atenolol	-	150				74.23		
MoS_2/MTT	Acebutolol	-	150	Adsorption capacity (mg g^{-1})			113.82		[114]
MoS_2	Acebutolol	-	150				36.05		
Photocatalysis									
Catalyst	**Contaminant**	**Band Gap (eV)**		**Specific Area (m^2/g)**	**Irradiation Time (min)**	**Removal Rate (%)**	**PFO Kinetics k (min^{-1})**		**Ref.**
MZO (MoS_2/ZnO)	MB	-		14.785	40	97	0.070		[121]
MoS_2	MB	-		3.795	40	44	0.010		
MoS_2/Fe_3O_4 (MF-17)	MB	-		4.5	120	98	-		[25]
MoS_2	MB	-		9.0	120	92	-		
MoS_2-TiO_2	MO	2.76		103.5	60	86	0.016		[127]
MoS_2	MO	3.26		88.5	60	53	0.008		
BiOI/MoS_2 (BMS-8)	RhB	BiOI 1.42 MoS_2 1.73		30.76	90	100	0.023		[3]
MoS_2	RhB	MoS_2 1.73		49.59	90	60	0.009		

Table 4. *Cont.*

Photocatalysis							
Catalyst	**Contaminant**	**Band Gap (eV)**	**Specific Area (m^2/g)**	**Irradiation Time (min)**	**Removal Rate (%)**	**PFO Kinetics k (min^{-1})**	**Ref.**
MoS_2/Fe_3O_4 (MF-17)	RhB	-	4.5	120	96	-	[25]
MoS_2	RhB	-	9.0	120	82	-	
MoS_2/TiO_2/graphene (MTG-48)	TC	3.17	58.6	60	92	0.05	[137]
MoS_2	TC	2.66	29.3	60	54	0.018	
MoS_2-ZnS	Crystal violet	-	-	40	98.5	41.26×10^{-3}	[132]
MoS_2	Crystal violet	-	-	40	60	24.23×10^{-3}	
MoS_2-TiO_2	4-Nitrophenol	2.76	103.5	60	97	0.024	[127]
MoS_2	4-Nitrophenol	3.26	88.5	60	59	0.009	
UiO-66/MoS_2 (UMS-0.15)	Lomefloxacin	-	37.176	90	87	37.176	[113]
MoS_2	Lomefloxacin	-	7.775	90	38.2	7.775	
MoS_2/CuO-25%	2-MBT	MoS_2 1.52 CuO 2.16	47	120	96	-	[142]
MoS_2	2-MBT	1.52	14.76	120	22	-	

Note: 2-MBT—2,4-D—2,4-dichlorophenoxyacetic acid; MB—methylene blue; MO—methyl orange; MMT—montmorillonite; RhB—rhodamine B; TC—tetracycline; W-DR-N-MoS_2—Widened Defect Rich Nano MoS_2.

The combination of MoS_2 with semiconducting phases has been explored, to improve photocatalytic activity. Quan et al. [121] coupled MoS_2 nanoflowers to ZnO nanoparticles and observed a considerable increase in the degradation rate of methylene blue compared with bare MoS_2, from 44% to 97%, when submitted to visible light ($\lambda > 420$ nm). Introducing the semiconductor ZnO resulted in an increased photoinduced electron transfer rate, leading to higher photocatalytic activity. ZnO also presents attractive characteristics, such as low cost, low toxicity, high chemical stability, and strong photosensitivity [121]. Mahalakshmi et al. [127] produced core@shell TiO_2@MoS_2 heterojunction composites via the one-step hydrothermal method. The photocatalytic activity of the resulting composite toward 4-nitrophenol was enhanced compared to the MoS_2 and TiO_2 used separately, due to a reduced band gap and efficient separation of the photogenerated electron-hole pairs. A similar strategy was reported for coupling MoS_2 and CuO, with improved separation of electron-hole pairs [142]. A Z-scheme heterojunction was produced that promoted the separation of the photogenerated carriers and may also increase the specific area and, consequently, the number of active sites [142]. BiOI nanoplates were also combined with MoS_2 nanosheets [3]. ZnS was combined with MoS_2 to increase the efficiency of photocarrier generation, increasing the removal of crystal violet dye using visible light ($\lambda > 420$ nm) [132]. Composites of MoS_2 with UiO-66 resulted in an enhanced specific area and in more active sites being available [113]. Several studies report the incorporation of magnetic nanostructures (e.g., magnetite—Fe_3O_4) to enhance the photocatalytic activity of MoS_2 [25,135]. This approach facilitates the separation of the nanocatalyst from the treated solution and increases the efficiency of the transport of photogenerated electrons, leading to a higher removal rate, even in the case of a lower specific area compared to bare MoS_2 [25].

7. Reuse of MoS_2-Based Composites for Adsorption and Photocatalysis

After interacting with the contaminated solution, the catalysts and adsorbents should then be collected and reused to reduce the quantity of produced materials and the associated costs. Importantly, the composite should maintain good adsorption/photoactivity when reused. Reusability studies have been performed to verify the efficiency of the composite after several cycles. At the end of each removal experiment, the sorbent/photocatalyst is collected through centrifugation or filtration and is washed off with water and ethanol or water alone, and then dried [121,124]. In this context, magnetic nanomaterials are advantageous because they are easily recovered using magnetic separation, which requires less energy [25,100,111,135].

Table 5 compares the evolution of the degradation rate via adsorption and photodegradation after several testing cycles. The MoS_2-based composites showed good adsorption when comparing the first and the last cycles [99,110–112]. The Au/MoS_2 composites also presented good adsorption after four consecutive cycles in a solution containing multiple ions, demonstrating their great potential for heavy metal ion removal [28]. Zhi et al. [109] reported a removal rate of > 95% after 10 reusing cycles for the adsorption of Hg(II). Several other studies report minor differences in adsorption capacity at the first and last adsorption cycles, regardless of the contaminant. Conversely, a marked decrease in the adsorption of the antibiotic ofloxacin was observed when the rGO-MoS_2 composite was reused [7]. The removal decreased from 92% to just 4% after 8 cycles, but the authors do not offer a possible explanation [7].

The reuse of MoS_2-based photocatalysts has also been investigated. However, often, the papers do not give detailed results of the reuse studies. Overall, the photocatalyst maintains good photocatalytic activity after several cycles. Yet, in some cases, significant decreases in the photodegradation rate were observed due to the oxidation of the photocatalyst [126].

Table 5. Reuse of MoS_2-based sorbents and photocatalysts.

Adsorption						
MoS_2-Based Composite	**Contaminant**	**Contact Time (min)**	**Removal 1st Cycle (%)**	**Number of Cycles**	**Removal after Last Cycle (%)**	**Ref.**
Au/Fe_3O_4/MoS_2CAs	Hg(II)	30	95–100	10	>95	[109]
MoS_2/Fe_3O_4	Hg(II)	-	100–95	5	identical	[111]
MoS_2-kaolin	Hg(II)	50	99	5	77	[98]
MoS_2-rGO	Hg(II)	7	100	6	85–90	[110]
MoS_2/MTT	Hg(II)	-	100	4	85.2	[99]
MoS_2/Fe_3O_4	Pb(II)	-	100–95	5	identical	[111]
MoS_2/LDC	Cr(VI)	30	99	4	90	[112]
chitosan-coated MoS_2 1:2	Au(III)	-	98.9	4	86.4	[28]
MoS_2-rGO	Ofloxacin	-	92	8	4	[7]
Photocatalysis						
MoS_2-Based Catalyst	**Contaminant**	**Irradiation Time (min)**	**Removal 1st Cycle (%)**	**Number of Cycles**	**Removal after Last Cycle (%)**	**Ref.**
α-Fe_2O_3/MoS_2QDs	MB	1 120	83 91	3	1min 65 120 min 75	[92]
MZO (MoS_2/ZnO)	MB	40	97	5	89.10	[121]
ZnO/MoS_2 8 h	MB	37.5	85	5	65	[124]
CM12 (Cu_2O/MoS_2)	MO	30	90	5	40	[126]
CoO/meso-CN/MoS_2(1%) (S6)	MO	60	84	5	80	[118]
Ni foam with ZnO/MoS_2	MO	10	92.7	4	86.9	[120]
5% MoS_2/ZnO	RhB	50	95	5	87	[93]
CTAB-MoS_2-P25	RhB	120	91	4	76	[130]
1.9% MoS_2/g-C_3N_4/PAN	RhB	120	48	4	43	[125]
BiOI/MoS_2 (BMS-8)	RhB	90	100	6	>90	[3]
g-C_3N_4/MoS_2/GO (AT3G15)	RhB	60	99	5	92	[131]
CoO/meso-CN/MoS_2(1%) (S6)	Methyl red	60	96	5	90	[118]
CoO/meso-CN/MoS_2(1%) (S6)	Congo red	60	95	5	88	[118]
MoS_2-ZnS	Crystal violet	40	98.5	4	90.5	[132]
MoS_2/g-C_3N_4/TiO_2	Malachite green	60	86	4	70	[133]
MoS_2/BiOBr/CF	TC	120	89.0	4	80.7	[134]
Fe_3O_4/MoS_2/$BiVO_4$ (FMB3)	TC	120	86.1	5	>80	[135]
MoS_2/Z-50	TC	120	96.8	5	87.2	[136]
20 wt% MS/BEuCN	TC	50	99	3	identical	[120]
MoS_2/TiO_2/graphene (MTG-48)	TC	60	92	5	85	[137]
MoS_2/ZnO QDs	TC	80	96	5	89	[138]
CdS/MoS_2/ZnO(CMZ)	Ofloxacin	90	89	4	70–75	[139]
UiO-66/MoS_2 (UMS-0.15)	Lomefloxacin	90	87	4	79	[113]
MXene-Ti_3C_2/MoS_2 (MT-4)	Ranitidine	60	88.4		80	[140]
RGO10%/ZnO20%/MoS_2	Aniline	120	100	5	100	[141]
MoS_2/CuO-25%	2-MBT	120	96	5	91	[142]
MoS_2/BiOBr/CF	Cr(VI)	120	84.7	4	76.6	[134]
MoS_2/TiO_2/graphene (MTG-48)	Pb(II)	60	88	6	80	[137]

Note: 2-MBT—2-mercaptobenzothiazole; CF—carbon fiber; CTAB—cetyltrimethyl ammonium bromide; LDC—lignin-derived carbon; MB—methylene blue; MO—methyl orange; MTT—montmorillonite; QDs—quantum dots; rGO—reduced graphene oxide; RhB—rhodamine B; TC—tetracycline.

8. Application of MoS_2-Based Composites in Real Environmental Samples

So far, most studies have only focused on treating singular contaminant solutions in synthetic aqueous samples. The number of reports testing MoS_2 and composites in water decontamination in more realistic conditions is still scarce. MoS_2/Fe_3O_4 composite was employed as an adsorbent to treat effluents from lead-acid battery factories, reaching a Pb(II) removal of 99.6% and showing acceptable Pb(II) removal in contaminated soil [111]. Regarding the adsorption of organic contaminants, Zeng et al. [147] used MoS_2-decorated biochar to remove the antibiotic tetracycline hydrochloride from river and tap water. The adsorption capacity was found to be higher in environmental water samples when compared to synthetic solutions, prepared in deionized water and used under the same conditions. Furthermore, the composite could be reused for 5 cycles with only a minor decrease in the adsorption capacity. Conversely, the adsorption capacity of the antibiotic ofloxacin by the rGO-MoS_2 composites in river water was lower than in deionized water [7]. The effect was ascribed to the presence of cations, natural and synthetic organic chemicals that compete with ofloxacin for adsorption, leading to a decrease in the adsorption capacity. Huang et al. [148] realized that the photocatalytic activity of MoS_2 microspheres in degrading thiobencarb in lake or river water decreased by 20% compared to its performance in spiked deionized water, under identical reaction conditions. The presence of anions in non-deionized water acting as scavengers was identified as a cause for the decrease in photocatalytic activity. Nevertheless, the authors considered this material a potential catalyst for removing pollutants. Chandrabose et al. [149] assessed the photocatalytic efficiency of MoS_2/TiO_2 composite in a solution comprising a mixture of anionic dyes (rhodamine B and methyl orange) and cationic dyes (methylene blue and crystal violet). The composite removed 100% of cationic dyes and 70% of the anionic dyes in the first stage of adsorption in the dark, while the remaining 30% of anionic dyes were photodegraded entirely after 3.5 h in a second stage under UV-Vis light irradiation. The composite showed higher adsorptive affinity to the cationic dyes compared to anionic dyes. Increasing contaminant concentrations resulted in less adsorptive removal at the first stage, which was limited by the surface area of the composite. The results of the study show the potential of using this MoS_2-based composite for the removal of dyes produced by textile industries.

9. Environmental Impact of MoS_2-Based Composites

Water remediation studies employing MoS_2-based composites have been focused on the evaluation and enhancement of the composites' removal capacity. The assessment of the ecotoxicity of the materials has been less widely investigated, although it is a fundamental matter. Nanomaterials have emerged as a promising tool for water remediation, but, due to their high surface area and chemical activity, if accidentally released into the environment, they may constitute a risk [150]. Depending on their chemical properties and composition, nanomaterials can be modified by oxidation, sulfidation, aggregation, and deposition in the natural environment [151]. In terms of the properties of nano-MoS_2, this material is considered chemically stable even in environmental conditions [75]. Due to its low solubility in water systems, it is also considered a persisting compound. Nano-MoS_2 may persist in the environment and the actual risks are still unknown. The nanosheets of MoS_2 showed antibacterial activity against *Escherichia coli* and *Staphylococcus aureus* and low cytotoxicity for Vero cells [19]. Cicuendez et al. [152] also observed good viability of mouse and human cells when exposed to MoS_2 flakes. A more comprehensive study on the toxicity of bulk and MoS_2 nanosheets was conducted to address the toxicity in various aquatic species of different taxonomic groups [34]. The EC50 was determined for four species: *Vibrio fischeri*, a marine Gram-negative photobacterium, *Pseudokirchnerialla subcapitata*, a freshwater microalga, *Daphnia magna*, a freshwater crustacean, and *Spirodela polyrhiza*, a freshwater duckweed. Bulk and nano MoS_2 (0.05–2.00 g/L) were tested for a contact time ranging from 15 min to 72 h. It was found that bulk MoS_2 was more toxic than MoS_2

nanosheets for all the species tested; in some cases, nano MoS_2 showed no toxicity for the tested conditions.

10. Conclusions and Perspectives

In summary, this review highlights the advantages of MoS_2 and MoS_2–based nanomaterials for water treatment applications through adsorption and photocatalysis. Owing to the high surface area and visible light-responsive photocatalytic activity, we can expect growing interest in these materials for environmental applications in the near future. Several advances have been made in synthetic methods for the production of MoS_2 nanomaterials with different structural features, namely, the crystal phase, morphology and layer spacing, which each create distinct physicochemical properties. The applications of MoS_2 and composites in the adsorption and photodegradation of metal ion species and organic contaminants are thoroughly summarized. The modification of MoS_2 and its combination with other components enhance those properties that increase removal efficiency and may also facilitate the separation of the catalyst from the solution. Despite the progress achieved, more studies are needed to rationally fabricate highly efficient MoS_2-based photocatalysts, which represents an opportunity for further research efforts. The ecotoxicity of MoS_2 is still not clear and requires further investigation. Although MoS_2 presents high chemical stability, even in environmental aqueous systems, it also presents some toxicity to different organisms. More studies should be conducted to assess the risks of employing MoS_2-based materials in water treatment.

Author Contributions: Conceptualization, L.O.A. and A.L.D.-d.-S.; methodology, L.O.A. and A.L.D.-d.-S.; investigation, L.O.A.; writing—original draft preparation, L.O.A.; writing—review and editing, L.O.A. and A.L.D.-d.-S.; supervision, A.L.D.-d.-S.; funding acquisition, A.L.D.-d.-S. All authors have read and agreed to the published version of the manuscript.

Funding: L. O. Amaral thanks the Fundação para a Ciência e Tecnologia (FCT) for Ph.D. grant number UI/BD/151138/2021. This work was developed within the scope of the project CICECO-Aveiro Institute of Materials, UIDB/50011/2020, UIDP/50011/2020, and LA/P/0006/2020, financed by national funds through the FCT/MCTES (PIDDAC).

Institutional Review Board Statement: Not applicable.

Informed Consent Statement: Not applicable.

Data Availability Statement: Not applicable.

Conflicts of Interest: The authors declare no conflict of interest.

References

1. Yang, D.; Yang, Y.; Xia, J. Hydrological cycle and water resources in a changing world: A review. *Geogr. Sustain.* **2021**, *2*, 115–122. [CrossRef]
2. Chen, X.; Shuai, C.; Wu, Y.; Zhang, Y. Understanding the sustainable consumption of energy resources in global industrial sector: Evidences from 114 countries. *Environ. Impact Assess. Rev.* **2021**, *90*, 106609. [CrossRef]
3. Hao, L.; Ju, P.; Zhang, Y.; Zhai, X.; Sun, C.; Duan, J.; Su, Y.; Lu, Z.; Liao, D. Fabrication of hierarchical flower-like BiOI/MoS_2 heterostructures with highly enhanced visible-light photocatalytic activities. *Colloids Surf. A Physicochem. Eng. Asp.* **2021**, *610*, 125714. [CrossRef]
4. Liu, Y.; Ma, C.; Zhang, X.; Ngo, H.N.; Guo, W.; Zhang, M.; Zhang, D. Role of structural characteristics of MoS_2 nanosheets on Pb^{2+} removal in aqueous solution. *Environ. Technol. Innov.* **2021**, *22*, 101385. [CrossRef]
5. Shahid, M.K.; Kashif, A.; Fuwad, A.; Choi, Y. Current advances in treatment technologies for removal of emerging contaminants from water—A critical review. *Coord. Chem. Rev.* **2021**, *442*, 101385. [CrossRef]
6. Soares, S.F.; Fernandes, T.; Trindade, T.; Daniel-da-Silva, A.L. Recent advances on magnetic biosorbents and their applications for water treatment. *Environ. Chem. Lett.* **2020**, *18*, 151–164. [CrossRef]
7. Jaswal, A.; Kaur, M.; Singh, S.; Kansal, S.K.; Umar, A.; Garoufalis, C.S.; Baskoutas, S. Adsorptive removal of antibiotic ofloxacin in aqueous phase using rGO-MoS_2 heterostructure. *J. Hazard. Mater.* **2021**, *417*, 125982. [CrossRef] [PubMed]
8. Pandey, S.; Fosso-Kankeu, E.; Spiro, M.J.; Waanders, F.; Kumar, N.; Ray, S.S.; Kim, J.; Kang, M. Equilibrium, kinetic, and thermodynamic studies of lead ion adsorption from mine wastewater onto MoS_2- clinoptilolite composite. *Mater. Today Chem.* **2020**, *18*, 100376. [CrossRef]

9. Estrada, A.C.; Daniel-da-Silva, A.L.; Leal, C.; Monteiro, C.; Lopes, C.B.; Nogueira, H.I.S.; Lopes, I.; Martins, M.J.; Martins, N.C.T.; Gonçalves, N.P.F.; et al. Colloidal nanomaterials for water quality improvement and monitoring. *Front. Chem.* **2022**, *10*, 1011186. [CrossRef]
10. Tan, C.; Cao, X.; Wu, X.J.; He, Q.; Yiang, J.; Zhang, X.; Chen, J.; Zhao, W.; Han, S.; Nam, G.H.; et al. Recent advances in ultrathin two-dimensional nanomaterials. *Chem. Rev.* **2017**, *117*, 6225–6331. [CrossRef]
11. Darvishi, M.; Foroutan, M. Molecular investigation of water adsorption on MoS_2 and graphene surfaces. *J. Mol. Liq.* **2017**, *225*, 1–10. [CrossRef]
12. Singh, A.; Shirodkar, S.N.; Waghmare, U.V. 1H and 1T polymorphs, structural transitions and anomalous properties of (Mo,W)$(S,Se)_2$ monolayers: First-principles analysis. *2D Mater.* **2015**, *2*, 035013. [CrossRef]
13. Liu, Y.; Zhao, Y.; Zhang, X.; Huang, X.; Liao, W.; Zhao, Y. MoS_2-based membranes in water treatment and purification. *Chem. Eng. J.* **2021**, *422*, 130082. [CrossRef]
14. Zhang, W.; Huang, J.K.; Chen, C.H.; Chang, Y.H.; Cheng, Y.J.; Li, L.J. High-gain phototransistors based on a CVD MoS_2 monolayer. *Adv. Mater.* **2013**, *25*, 3456–3461. [CrossRef] [PubMed]
15. Shan, J.; Li, J.; Chu, X.; Xu, M.; Jin, F.; Fang, X.; Wei, Z.; Wang, X. Enhanced photoresponse characteristics of transistors using CVD-grown MoS_2/WS_2 heterostructures. *Appl. Surf. Sci.* **2018**, *443*, 31–38. [CrossRef]
16. Christinelli, W.A.; Shimizu, F.M.; Facure, M.H.M.; Cerri, R.; Oliveira Jr, O.N.; Correa, D.S.; Mattoso, L.H.C. Two-dimensional MoS_2-based impedimetric electronic tongue for the discrimination of endocrine disrupting chemicals using machine learning. *Sens. Actuators B Chem.* **2021**, *336*, 129696. [CrossRef]
17. Raadnui, S.; Mahathanabodee, S.; Tongsri, R.; Morakotjinda, M.; Wila, P. Comparison of dry sliding tribological behavior of SS 316L impregnated with MoS_2 vs. h-BN solid lubricants: A statistical point of view. *Wear* **2021**, *476*, 203676. [CrossRef]
18. Dawari, C.K.; Haq, I.; Mönkkönen, K.; Suvanto, M.; Saarinen, J.J. Reduced sliding friction on flat and microstructured metal injection molded (MIM) WC-Co hard metals with MoS_2 composite lubricants. *Tribol. Int.* **2021**, *160*, 107020. [CrossRef]
19. Kasinathan, K.; Marimuthu, K.; Murigesan, B.; Pandiyan, N.; Pandi, B.; Mahalingam, S.; Selvaraj, B. Cyclodextrin functionalized multi-layered MoS_2 nanosheets and its biocidal activity against pathogenic bacteria and MCF-7 breast cancer cells: Synthesis, characterization and in-vitro biomedical evaluation. *J. Mol. Liq.* **2021**, *323*, 114631. [CrossRef]
20. Sha, R.; Bhattacharyya, T.K. MoS_2-based nanosensors in biomedical and environmental monitoring applications. *Electrochim. Acta.* **2020**, *349*, 136370. [CrossRef]
21. Kumar, R.R.; Murugesan, T.; Dash, A.; Hsu, C.; Gupta, S.; Manikandan, A.; Anbalagan, A.k.; Lee, C.; Tai, N.; Chueh, Y.; et al. Ultrasensitive and light-activated NO_2 gas sensor based on networked MoS_2/ZnO nanohybrid with adsorption/desorption kinetics study. *Appl. Surf. Sci.* **2021**, *536*, 147933. [CrossRef]
22. Zhang, Z.; Li, W.; Wang, R.; Li, H.; Yan, J.; Jin, Q.; Feng, P.; Wang, K.; Jiang, K. Crystal water assisting MoS_2 nanoflowers for reversible zinc storage. *J. Alloys. Compd.* **2021**, *872*, 159599. [CrossRef]
23. Zhang, L.; Mu, L.; Zhou, Q.; Hu, X. Solar-assisted fabrication of dimpled 2H-MoS_2 membrane for highly efficient water desalination. *Water Res.* **2020**, *170*, 115367. [CrossRef]
24. Peng, W.; Wang, W.; Qi, M.; Miao, Y.; Huang, Y.; Yu, F. Enhanced capacitive deionization of defect-containing MoS_2/graphene composites through introducing appropriate MoS_2 defect. *Electrochim. Acta.* **2021**, *383*, 138363. [CrossRef]
25. Wang, Q.; Dong, S.; Zhang, D.; Yu, C.; Lu, J.; Wang, D.; Sun, J. Magnetically recyclable visible-light responsive MoS_2@Fe_3O_4 photocatalysts targeting efficient wastewater treatment. *J. Mater. Sci.* **2018**, *53*, 1135–1147. [CrossRef]
26. Zhu, Q.; Xu, Q.; Du, M.; Zeng, X.; Zhong, G.; Qiu, B.; Zhang, J. Recent progress of metal sulfide photocatalysts for solar energy conversion. *Adv. Mater.* **2022**, 2202929. [CrossRef]
27. Hasija, V.; Raizada, P.; Thakur, V.K.; Parwaz Khan, A.A.; Asiri, A.M.; Singh, P. An overview of strategies for enhancement in photocatalytic oxidative ability of MoS_2 for water purification. *J. Environ. Chem. Eng.* **2020**, *8*, 104307. [CrossRef]
28. Zhao, M.; Huang, Z.; Wang, S.; Zhang, L. Ultrahigh efficient and selective adsorption of Au(III) from water by novel Chitosan-coated MoS_2 biosorbents: Performance and mechanisms. *Chem. Eng. J.* **2020**, *401*, 126006. [CrossRef]
29. Yang, X.; Li, J.; Liang, T.; Ma, C.; Zhang, Y.; Chen, H.; Hanagata, N.; Su, H.; Xu, M. Antibacterial activity of two-dimensional MoS2 sheets. *Nanoscale* **2014**, *6*, 10126–10133. [CrossRef]
30. Fan, J.; Li, Y.; Nguyen, H.N.; Yao, Y.; Rodrigues, D.F. Toxicity of exfoliated-MoS_2 and annealed exfoliated-MoS_2 towards planktonic cells, biofilms, and mammalian cells in the presence of electron donor. *Environ. Sci. Nano.* **2015**, *2*, 370–379. [CrossRef]
31. Cheng, A.; Zhang, H.; Zhong, W.; Li, Z.; Tang, Y.; Li, Z. Enhanced electrochemical properties of single-layer MoS_2 embedded in carbon nanofibers by electrospinning as anode materials for sodium-ion batteries. *J. Electroanal. Chem.* **2019**, *843*, 31–36. [CrossRef]
32. Zhao, P.; Zheng, J.; Guo, P.; Jiang, Z.; Cao, L.; Wan, Y. Electronic and magnetic properties of Re-doped single-layer MoS_2: A DFT study. *Comput. Mater. Sci.* **2017**, *128*, 287–293. [CrossRef]
33. Gangwar, R.; Pandey, D.; Kancharlapalli, S.; Raychaudhuri, D.; Chakrabarti, A.; Banerjee, A.; Ghanti, T.K. Ab Initio Study of Adsorption of Fission Gas Atoms Xe and Kr on MoS_2 Monolayer Functionalized with 3d Transition Metals. *J. Phys. Chem. C.* **2021**, *125*, 1493–1508. [CrossRef]
34. Arefi-Oskoui, S.; Khataee, A.; Ucun, O.K.; Kobya, M.; Hanci, T.Ö.; Arslan-Alaton, I. Toxicity evaluation of bulk and nanosheet MoS_2 catalysts using battery bioassays. *Chemosphere* **2021**, *268*, 128822. [CrossRef]
35. Rani, A.; Singh, K.; Patel, A.S.; Chakraborti, A.; Kumar, S.; Ghosh, K.; Sharma, P. Visible light driven photocatalysis of organic dyes using SnO_2 decorated MoS_2 nanocomposites. *Chem. Phys. Lett.* **2020**, *738*, 136874. [CrossRef]

36. Chang, M.J.; Cui, W.N.; Liu, J.; Wang, K.; Du, H.L.; Qiu, L.; Fan, S.M.; Luo, Z.M. Construction of novel $TiO_2/Bi_4Ti_3O_{12}/MoS_2$ core/shell nanofibers for enhanced visible light photocatalysis. *J. Mater. Sci. Technol.* **2020**, *36*, 97–105. [CrossRef]
37. Eda, G.; Yamaguchi, H.; Voiry, D.; Fujita, T.; Chen, M.; Chhowalla, M. Photoluminescence from chemically exfoliated MoS_2. *Nano Lett.* **2011**, *11*, 5111–5116. [CrossRef]
38. Radisavljevic, B.; Radenovic, A.; Brivio, J.; Giacometti, V.; Kis, A. Single-layer MoS_2 transistors. *Nat. Nanotechnol.* **2011**, *6*, 147–150. [CrossRef]
39. Han, Y.; Chen, P.; Zhang, C.; Dong, J.; Liu, H. The buckling behavior of single-layer MoS_2 sheets with kirigami-inspired structures under compression. *Comput. Mater. Sci.* **2021**, *188*, 110188. [CrossRef]
40. Splendiani, A.; Sun, L.; Zhang, Y.; Li, T.; Kim, J.; Chim, C.Y.; Galli, G.; Wang, F. Emerging photoluminescence in monolayer MoS_2. *Nano Lett.* **2010**, *10*, 1271–1275. [CrossRef]
41. Han, B.; Hu, Y.H. MoS_2 as a co-catalyst for photocatalytic hydrogen production from water. *Energy Sci. Eng.* **2016**, *4*, 285–304. [CrossRef]
42. Szary, M.J.; Michalewicz, M.T.; Radny, M.W. Giant spin splitting induced by a symmetry-braking van der Waals interaction. *Appl. Surf. Sci.* **2019**, *494*, 619–626. [CrossRef]
43. Kumar, S.; Mishra, T. Shock wave induced exfoliation of molybdenum disulfide (MoS_2) in various solvents: All-atom molecular dynamics simulation. *J. Mol. Liq.* **2020**, *314*, 113671. [CrossRef]
44. Zhao, X.; Ning, S.; Fu, W.; Pennycook, S.J.; Loh, K.P. Differentiating polymorphs in molybdenum disulfide via electron microscopy. *Adv. Mater.* **2018**, *30*, 1802397. [CrossRef]
45. Szary, M.J. Al doped MoS_2 for adsorption-based water collection. *Appl. Surf. Sci.* **2020**, *529*, 147083. [CrossRef]
46. Ramsdell, L.S. Studies on silicon carbide. *Am. Mineral.* **1947**, *32*, 64–82.
47. Krishnan, U.; Kaur, M.; Singh, K.; Kumar, M.; Kumar, A. A synoptic review of MoS_2: Synthesis to applications. *Superlattices Microstruct.* **2019**, *128*, 274–297. [CrossRef]
48. Wang, Z.; Mi, B. Environmental Applications of 2D Molybdenum Disulfide (MoS_2) Nanosheets. *Environ. Sci. Technol.* **2017**, *51*, 8229–8244. [CrossRef]
49. Singh, A.K.; Kumar, P.; Late, D.J.; Kumar, A.; Patel, S.; Singh, J. 2D layered transition metal dichalcogenides (MoS_2): Synthesis, applications and theoretical aspects. *Appl. Mater. Today* **2018**, *13*, 242–270. [CrossRef]
50. Evans, P.E.; Komesu, T.; Schwier, E.F.; Kumar, S.; Shimada, K.; Dowben, P.A. The band shifts in $MoS_2(0001)$ and $WSe_2(0001)$ induced by palladium adsorption. *J. Phys. Condens. Matter.* **2020**, *32*, 465001. [CrossRef]
51. Yun, W.S.; Han, S.W.; Hong, S.C.; Kim, I.G.; Lee, J.D. Thickness and strain effects on electronic structures of transition metal dichalcogenides: 2H-MX_2 semiconductors (M = Mo, W, X = S, Se, Te). *Phys. Rev. B Condens. Matter. Mater. Phys.* **2012**, *85*, 033305. [CrossRef]
52. Tang, Q.; Jiang, D.E. Mechanism of hydrogen evolution reaction on 1T-MoS_2 from first principles. *ACS Catal.* **2016**, *6*, 4953–4961. [CrossRef]
53. Liu, Q.; Fang, Q.; Chu, W.; Wan, Y.; Li, X.; Xu, W.; Habib, M.; Tao, S.; Zhou, Y.; Liu, D.; et al. Electron-doped 1T-MoS_2 via interface engineering for enhanced electrocatalytic hydrogen evolution. *Chem. Mater.* **2017**, *29*, 4738–4744. [CrossRef]
54. Hu, T.; Li, R.; Dong, J. A new (2×1) dimerized structure of monolayer 1T-molybdenum disulfide, studied from first principles calculations. *J. Chem. Phys.* **2013**, *139*, 174702. [CrossRef]
55. Wu, M.H.; Li, L.; Liu, N.; Wang, D.J.; Xue, Y.C.; Tang, L. Molybdenum disulfide (MoS_2) as a co-catalyst for photocatalytic degradation of organic contaminants: A review. *Process Saf. Environ. Prot.* **2018**, *118*, 40–58.
56. Kour, P.; Deeksha; Yadav, K. Electrochemical performance of mixed-phase 1T/2H MoS_2 synthesized by conventional hydrothermal v/s microwave-assisted hydrothermal method for supercapacitor applications. *J. Alloys. Compd.* **2022**, *922*, 166194. [CrossRef]
57. Mishra, S.; Maurya, P.K.; Mishra, A.K. 2H–MoS_2 nanoflowers based high energy density solid state supercapacitor. *Mater Chem Phys.* **2020**, *255*, 123551. [CrossRef]
58. Nie, C.; Yin, M.; Zhao, Y.; Zhao, C.; Zhang, B.; Song, X.; Yi, X.; Zhang, Y.; Luo, L.; Wang, S. Tailoring the fluorescent and electronic properties of 2H-MoS_2 by step-by-step functionalization. *J. Phys. Chem. C* **2021**, *125*, 25739–25748. [CrossRef]
59. Li, F.; Shen, T.; Xu, L.; Hu, C.; Qi, J. Strain improving the performance of a flexible monolayer MoS_2 photodetector. *Adv Electron Mater.* **2019**, *5*, 1900803. [CrossRef]
60. Bai, H.; Wu, Q.; Ai, H.; Liu, D.; Feng, J.; Ang, L.K.; Lu, Y.; Yang, M.; Pan, H. Interlayer-incorporation of MoS_2 (TM-MoS_2) to achieve unique magnetic and electronic properties for spintronics. *Adv. Electron. Mater.* **2022**, 2200209. [CrossRef]
61. Panasci, S.E.; Koos, A.; Schilirò, E.; Di Franco, S.; Greco, G.; Fiorenza, P.; Roccaforte, F.; Agnello, S.; Cannas, M.; Gelardi, F.M.; et al. Multiscale investigation of the structural, electrical and photoluminescence properties of MoS_2 obtained by MoO_3 sulfurization. *Nanomaterials* **2022**, *12*, 182. [CrossRef] [PubMed]
62. Pradhan, G.; Sharma, A.K. Temperature controlled 1T/2H phase ratio modulation in mono- and a few layered MoS_2 films. *Appl. Surf. Sci.* **2019**, *479*, 1236–1245. [CrossRef]
63. Silambarasan, K.; Archana, J.; Harish, S.; Navaneethan, M.; Ganesh, R.S.; Ponnusamy, S.; Muthamizhchelvan, C.; Hara, K. One-step fabrication of ultrathin layered 1T@2H phase MoS_2 with high catalytic activity based counter electrode for photovoltaic devices. *J. Mater. Sci. Technol.* **2020**, *51*, 94–101.
64. Tan, D.; Willatzen, M.; Wang, Z.L. Prediction of strong piezoelectricity in 3R-MoS_2 multilayer structures. *Nano Energy* **2018**, *56*, 512–515. [CrossRef]

65. Strachan, J.; Masters, A.F.; Maschmeyer, T. 3R-MoS_2 in review: History, status, and outlook. *ACS Appl. Energy Mater.* **2021**, *4*, 7405–7418. [CrossRef]
66. Shi, J.; Yu, P.; Liu, F.; He, P.; Wang, R.; Qin, L.; Zhou, J.; Li, X.; Zhou, J.; Sui, X.; et al. 3R MoS_2 with broken inversion symmetry: A promising ultrathin nonlinear optical device. *Adv. Mater.* **2017**, *29*, 1701486. [CrossRef] [PubMed]
67. Anghel, S.; Chumakov, Y.; Kravtsov, V.; Volodina, G.; Mitioglu, A.; Plochocka, P.; Sushkevich, K.; Mishina, E.; Kulyuk, L. Site-selective luminescence spectroscopy of bound excitons and local band structure of chlorine intercalated 2H- and 3R-MoS_2 polytypes. *J. Lumin.* **2016**, *177*, 331–336. [CrossRef]
68. Chen, J.; Zhao, X.; Grinblat, G.; Chen, Z.; Tan, S.J.R.; Fu, W.; Ding, Z.; Abdelwahab, I.; Li, Y.; Geng, D.; et al. Homoepitaxial growth of large-scale highly organized transition metal dichalcogenide patterns. *Adv. Mater.* **2018**, *30*, 1704674. [CrossRef]
69. Saber, M.R.; Khabiri, G.; Maarouf, A.A.; Ulbricht, M.; Khalil, A.S.G. A comparative study on the photocatalytic degradation of organic dyes using hybridized 1T/2H, 1T/3R and 2H MoS_2 nano-sheets. *RSC Adv.* **2018**, *8*, 26364–26370. [CrossRef] [PubMed]
70. Chen, J.; Cao, J.; Zhou, J.; Wang, W.; Zhang, Y.; Liu, X. Computational screening for enhanced hydrogen sensing by doped-2H and pristine-1T MoS_2. *Chem. Phys. Lett.* **2020**, *749*, 137450. [CrossRef]
71. Ma, J.; Zhang, Q.; Yang, J.; Feng, S.; Lei, M.; Quhe, R. Computational study of phase engineered transition metal dichalcogenides heterostructures. *Comput. Mater. Sci.* **2018**, *142*, 129–134. [CrossRef]
72. Xiao, Y.; Tan, M.; Li, Z.; He, L.; Gao, B.; Chen, Y.; Zheng, Y.; Lin, B. Ethylenediamine-assisted phase engineering of 1T/2H–MoS_2/graphene for efficient and stable electrocatalytic hydrogen evolution. *Int. J. Hydrog. Energy* **2021**, *46*, 11688–11700. [CrossRef]
73. Pirarath, R.; Shivashanmugam, P.; Syed, A.; Elgorban, A.M.; Anandan, S.; Ashokkumar, M. Mercury removal from aqueous solution using petal-like MoS_2 nanosheets. *Front. Environ. Sci. Eng.* **2021**, *15*, 1–10. [CrossRef]
74. Zeng, M.; Yang, B.; Yan, H.; Qu, H.; Hu, Y. Efficient recovery of Ag(I) from aqueous solution using MoS_2 nanosheets: Adsorption study and DFT calculation. *Chem. Phys. Lett.* **2020**, *757*, 137865. [CrossRef]
75. Wang, Z.; Zhu, W.; Qiu, Y.; Yi, X.; Bussche, A.; Kane, A.; Gao, H.; Koski, K.; Hurt, R. Biological and environmental interactions of emerging two-dimensional nanomaterials. *Chem. Soc. Rev.* **2016**, *45*, 1750–1780. [CrossRef] [PubMed]
76. Wu, P.R.; Liu, Z.; Cheng, Z.L. A top-down exfoliation for MoS_2 nanosheets based on Li^+/Na^+ -intercalated and shearing synergistic process. *Mater. Lett.* **2019**, *248*, 236–240. [CrossRef]
77. Deepak, D.R.; Nair, M.G.; Halder, S.; Sharma, A.L.; Mohapatra, S.R. Liquid phase exfoliation of MoS_2 nano-sheets and observation of resistive switching memory in MoS_2 Nano-sheets-PVDF-HFP composite films. *Mater. Today Proc.* **2019**, *18*, 5447–5453. [CrossRef]
78. Hai, N.Q.; Kwon, S.H.; Kim, H.; Kim, I.T.; Lee, S.G.; Hur, J. High-performance MoS_2-based nanocomposite anode prepared by high-energy mechanical milling: The effect of carbonaceous matrix on MoS_2. *Electrochim. Acta.* **2018**, *260*, 129–138. [CrossRef]
79. Li, Y.; Yin, X.; Huang, X.; Liu, X.; Wu, W. Efficient and scalable preparation of MoS_2 nanosheet/carbon nanotube composites for hydrogen evolution reaction. *Int. J. Hydrog. Energy* **2020**, *45*, 16489–16499. [CrossRef]
80. Yang, X.; Chen, Z.; Fang, J.; Yang, Q.; Zhao, W.; Qian, X.; Liu, C.; Zhou, D.; Tao, S.; Liu, X. Efficient exfoliation to MoS_2 nanosheets by salt-assisted refluxing and ultrasonication with photocatalytic application. *Mater. Lett.* **2019**, *255*, 126596. [CrossRef]
81. Tsigkourakos, M.; Kainourgiaki, M.; Skotadis, E.; Giannakopoulos, K.P.; Tsoukalas, D.; Raptis, Y.S. Capping technique for chemical vapor deposition of large and uniform MoS_2 flakes. *Thin Solid Film* **2021**, *733*, 138808. [CrossRef]
82. Luo, S.; Cullen, C.P.; Guo, G.; Zhong, J.; Duesberg, G.S. Investigation of growth-induced strain in monolayer MoS_2 grown by chemical vapor deposition. *Appl. Surf. Sci.* **2020**, *508*, 145126. [CrossRef]
83. Luo, L.; Shi, M.; Zhao, S.; Tan, W.; Lin, X.; Wang, H.; Jiang, F. Hydrothermal synthesis of MoS_2 with controllable morphologies and its adsorption properties for bisphenol A. *J. Saudi Chem. Soc.* **2019**, *23*, 762–773. [CrossRef]
84. Shan, J.; Li, J.; Chu, X.; Xu, M.; Jin, F.; Wang, X.; Ma, L.; Fang, X.; Wei, Z.; Wang, X. High sensitivity glucose detection at extremely low concentrations using a MoS_2-based field-effect transistor. *RSC Adv.* **2018**, *8*, 7942–7948. [CrossRef] [PubMed]
85. Ambrosi, A.; Chia, X.; Sofer, Z.; Pumera, M. Enhancement of electrochemical and catalytic properties of MoS_2 through ball-milling. *Electrochem. Commun.* **2015**, *54*, 36–40. [CrossRef]
86. Tayyebi, A.; Ogino, N.; Hayashi, T.; Komatsu, N. Size-controlled MoS_2 nanosheet through ball milling exfoliation: Parameter optimization, structural characterization and electrocatalytic application. *Nanotechnology* **2020**, *31*, 75704. [CrossRef]
87. Ma, H.; Ben, S.; Shen, Z.; Zhang, X.; Wu, C.; Liao, S.; An, F. Investigating the exfoliation behavior of MoS_2 and graphite in water: A comparative study. *Appl. Surf. Sci.* **2020**, *512*, 145588. [CrossRef]
88. Manamel, L.T.; Mukherjee, A.; Das, B.C. Two-dimensional nanohybrid of MoS_2 and Rose Bengal: Facile solution growth and band structure probing. *Appl. Surf. Sci.* **2020**, *530*, 147063. [CrossRef]
89. Singla, R.; Kumar, S.; Hackett, T.A.; Reshak, A.H.; Kashyap, M.K. Genesis of magnetism in graphene/MoS_2 van der Waals heterostructures via interface engineering using Cr-adsorption. *J. Alloys Compd.* **2021**, *859*, 157776. [CrossRef]
90. Li, H.; Zhu, X.; Tang, Z.K.; Zhang, X.H. Low-temperature photoluminescence emission of monolayer MoS_2 on diverse substrates grown by CVD. *J. Lumin.* **2018**, *199*, 210–215. [CrossRef]
91. Park, H.J.; Kim, M.S.; Kim, J.; Joo, J. Photo-responsive transistors of CVD grown single-layer MoS_2 and its nanoscale optical characteristics. *Curr. Appl. Physics* **2016**, *16*, 1320–1325. [CrossRef]

92. Khabiri, G.; Aboraia, A.M.; Soliman, M.; Guda, A.A.; Butova, V.V.; Yahia, I.S.; Soldatov, A.V. A novel α-Fe_2O_3@MoS_2QDs heterostructure for enhanced visible-light photocatalytic performance using ultrasonication approach. *Ceram. Int.* **2020**, *46*, 19600–19608. [CrossRef]
93. Gang, R.; Xu, L.; Xia, Y.; Cai, J.; Zhan, L.; Wang, S.; Li, R. Fabrication of MoS_2 QDs/ZnO nanosheet 0D/2D heterojunction photocatalysts for organic dyes and gaseous heavy metal removal. *J. Colloid. Interface Sci.* **2020**, *579*, 853–861. [CrossRef]
94. Wang, H.; Zhou, Y.; Xing, H.; Yang, X.; Zong, Y.; Feng, J.; Zhu, X.; Shi, Z.; Li, X.; Zheng, X. Construction of flower-like core-shell Fe_3O_4@2H-MoS_2 heterostructures: Boosting the interfacial polarization for high-performance microwave absorption. *Ceram Int.* **2022**, *48*, 9918–9926. [CrossRef]
95. Wu, Y.; Su, M.; Chen, J.; Xu, Z.; Tang, J.; Chang, X.; Chen, D. Superior adsorption of methyl orange by h-MoS_2 microspheres: Isotherm, kinetics, and thermodynamic studies. *Dye. Pigment.* **2019**, *170*, 1–8. [CrossRef]
96. Liu, P.; Cai, S.; Zuo, Y.; Tian, M.; Wang, Z.; Ling, L.; Sun, X. Synthesis of interlayer expanded MoS_2 by sulfurization of MoO_3 with enhanced sodium-ion storage. *J Alloys Compd.* **2022**, *895*, 162691. [CrossRef]
97. Ai, K.; Ruan, C.; Shen, M.; Lu, L. MoS_2 nanosheets with widened interlayer spacing for high-efficiency removal of mercury in aquatic systems. *Adv. Funct. Mater.* **2016**, *26*, 5542–5549. [CrossRef]
98. Yuan, W.; Kuang, J.; Yu, M.; Huang, Z.; Zou, Z.; Zhu, L. Facile preparation of MoS_2@Kaolin composite by one-step hydrothermal method for efficient removal of Pb(II). *J. Hazard. Mater.* **2021**, *405*, 124261. [CrossRef]
99. Mário, E.D.A.; Liu, C.; Ezugwu, C.I.; Mao, S.; Jia, F.; Song, S. Molybdenum disulfide/montmorillonite composite as a highly efficient adsorbent for mercury removal from wastewater. *Appl. Clay. Sci.* **2020**, *184*, 105370. [CrossRef]
100. Song, H.J.; You, S.; Jia, X.H.; Yang, J. MoS_2 nanosheets decorated with magnetic Fe_3O_4 nanoparticles and their ultrafast adsorption for wastewater treatment. *Ceram. Int.* **2015**, *41*, 13896–13902. [CrossRef]
101. Chen, Y.; Song, B.; Tang, X.; Lu, L.; Xue, J. Ultrasmall Fe_3O_4 nanoparticle/MoS_2 nanosheet composites with superior performances for lithium ion batteries. *Small* **2014**, *10*, 1536–1543. [CrossRef] [PubMed]
102. Xin, X.; Song, Y.; Guo, S.; Zhang, Y.; Wang, B.; Wang, Y.; Li, X. One-step synthesis of P-doped MoS_2 for efficient photocatalytic hydrogen production. *J. Alloys. Compd.* **2020**, *829*, 154635. [CrossRef]
103. Liu, F.; Wang, N.; Shi, C.; Sha, J.; Ma, L.; Liu, E.; Zhao, N. Phosphorus doping of 3D structural MoS_2 to promote catalytic activity for lithium-sulfur batteries. *Chem. Eng. J.* **2022**, *431*, 133923. [CrossRef]
104. Li, J.; He, T.; Zhao, Y.; Zhang, X.; Zhong, W.; Zhang, X.; Ren, J.; Chen, Y. In-situ N-doped ultrathin MoS_2 anchored on N-doped carbon nanotubes skeleton by Mo-N bonds for fast pseudocapacitive sodium storage. *J Alloys Compd.* **2022**, *897*, 163170. [CrossRef]
105. Zhang, Z.; Dong, Y.; Liu, G.; Li, J.; Sun, H.; Luo, H.; Liu, S. The ultrafine monolayer 1 T/2H-MoS_2: Preparation, characterization and amazing photocatalytic characteristics. *Colloids Surf. A Phys. Eng. Asp.* **2020**, *589*, 124431. [CrossRef]
106. Luo, N.; Chen, C.; Yang, D.; Hu, W.; Dong, F. S defect-rich ultrathin 2D MoS_2: The role of S point-defects and S stripping-defects in the removal of Cr(VI) via synergistic adsorption and photocatalysis. *Appl. Catal. B.* **2021**, *299*, 120664. [CrossRef]
107. Liu, S.; Nie, C.; Zhou, D.; Shen, J.; Feng, S. Direct growth of vertical structure MoS_2 nanosheets array film via CVD method for photodetection. *Physica E Low Dimens. Syst. Nanostruct.* **2020**, *117*, 113592. [CrossRef]
108. Cui, B.; Cai, X.; Wang, W.; Saha, P.; Wang, G. Nano storage-boxes constructed by the vertical growth of MoS_2 on graphene for high-performance Li-S batteries. *J. Energy Chem.* **2022**, *66*, 91–99. [CrossRef]
109. Zhi, L.; Zuo, W.; Chen, F.; Wang, B. 3D MoS_2 composition aerogels as chemosensors and adsorbents for colorimetric detection and high-capacity adsorption of Hg^{2+}. *ACS Sustain. Chem. Eng.* **2016**, *4*, 3398–3408. [CrossRef]
110. Zhuang, Y.T.; Zhang, X.; Wang, D.H.; Yu, Y.L.; Wang, J.H. Three-dimensional molybdenum disulfide/graphene hydrogel with tunable heterointerfaces for high selective Hg(II) scavenging. *J. Colloid. Interface Sci.* **2018**, *514*, 715–722. [CrossRef]
111. Wang, Z.; Zhang, J.; Wen, T.; Liu, X.; Wang, Y.; Yang, H.; Sun, J.; Feng, J.; Dong, S.; Sun, J. Highly effective remediation of Pb(II) and Hg(II) contaminated wastewater and soil by flower-like magnetic MoS_2 nanohybrid. *Sci. Total Environ.* **2020**, *699*, 134341. [CrossRef] [PubMed]
112. Chen, H.; Zhang, Z.; Zhong, X.; Zhuo, Z.; Tian, S.; Fu, S.; Chen, Y.; Liu, Y. Constructing MoS_2/Lignin derived carbon nanocomposites for highly efficient removal of Cr(VI) from aqueous environment. *J. Hazard. Mater.* **2021**, *408*, 124847. [CrossRef] [PubMed]
113. Gao, D.; Zhang, Y.; Yan, H.; Li, B.; He, Y.; Song, P.; Wang, R. Construction of UiO-66@MoS_2 flowerlike hybrids through electrostatically induced self-assembly with enhanced photodegradation activity towards lomefloxacin. *Sep. Purif. Technol.* **2021**, *265*, 118486. [CrossRef]
114. Shi, W.; Chu, Y.; Xia, M.; Wang, F.; Fu, C. The adsorption performance and micro-mechanism of MoS_2/montmorillonite composite to atenolol and acebutolol: Adsorption experiments and a novel visual study of interaction. *Ecotoxicol. Environ. Saf.* **2021**, *213*, 111993. [CrossRef] [PubMed]
115. Jayadharan Salini, A.N.; Ramachandran, A.; Sadasivakurup, S.; Yesodha, S.K. Versatile MoS_2 hollow nanoroses for a quick-witted removal of Hg (II), Pb (II) and Ag (I) from water and the mechanism: Affinity or Electrochemistry? *Appl. Mater. Today* **2020**, *20*, 100642. [CrossRef]
116. Prieto-Rodriguez, L.; Miralles-Cuevas, S.; Oller, I.; Agüera, A.; Puma, G.L.; Malato, S. Treatment of emerging contaminants in wastewater treatment plants (WWTP) effluents by solar photocatalysis using low TiO_2 concentrations. *J. Hazard. Mater.* **2012**, *211–212*, 131–137. [CrossRef] [PubMed]

117. Yuan, Y.J.; Lu, H.W.; Yu, Z.T.; Zou, Z.G. Noble-metal-free molybdenum disulfide cocatalyst for photocatalytic hydrogen production. *Chem. Sus. Chem.* **2015**, *8*, 4113–4127. [CrossRef]
118. Chen, L.; Chuang, Y.; Nguyen, T.B.; Chang, J.H.; Lam, S.S.; Chen, C.W.; Dong, C.D. Novel molybdenum disulfide heterostructure nanohybrids with enhanced visible-light-induced photocatalytic activity towards organic dyes. *J. Alloys. Compd.* **2020**, *848*, 156448. [CrossRef]
119. Abraham, T.; Priyanka, R.N.; Joseph, S.; Plathanam, N.J.; Gigimol, M.G.; Mathew, B. Flower-like $MoS_2/BiFeO_3$ doped silver orthophosphate catalyst for visible-light assisted treatment of refractory organic pollutants. *Appl. Mater. Today* **2020**, *21*, 100845. [CrossRef]
120. Fu, Y.; Ren, Z.; Wu, J.; Li, Y.; Liu, W.; Li, P.; Xing, L.; Ma, J.; Wang, H.; Xue, X. Direct Z-scheme heterojunction of ZnO/MoS_2 nanoarrays realized by flowing-induced piezoelectric field for enhanced sunlight photocatalytic performances. *Appl. Catal. B Environ.* **2021**, *285*, 119785. [CrossRef]
121. Quan, Y.; Su, R.; Hu, M.; Lang, J.; Fan, H.; Shen, H.; Gao, M.; Li, B.; Liu, Y.; Yang, J. Construction of an MZO heterojunction system with improved photocatalytic activity for degradation of organic dyes. *Cryst. Eng. Comm.* **2020**, *22*, 7059–7065. [CrossRef]
122. Guo, P.; Zhao, F.; Hu, X. Fabrication of a direct Z-scheme heterojunction between MoS_2 and B/Eu-g- C_3N_4 for an enhanced photocatalytic performance toward tetracycline degradation. *J. Alloys. Compd.* **2021**, *867*, 159044. [CrossRef]
123. Ahamad, T.; Naushad, M.; Alzaharani, Y.; Alshehri, S.M. Photocatalytic degradation of bisphenol-A with $g\text{-}C_3N_4/MoS_2$-PANI nanocomposite: Kinetics, main active species, intermediates and pathways. *J. Mol. Liq.* **2020**, *311*, 113339. [CrossRef]
124. Putritama, V.; Fauzia, V.; Supangat, A. The effect of the layer number of MoS_2 nanosheets on the photocatalytic efficiency of ZnO/MoS_2. *Surf. Interfaces* **2020**, *21*, 100745. [CrossRef]
125. Liang, H.; Bai, J.; Xu, T.; Li, C. Enhancing photocatalytic performance of heterostructure $MoS_2/g\text{-}C_3N_4$ embeded in PAN frameworks by electrospining process. *Mater. Sci. Semicond. Process* **2021**, *121*, 105414. [CrossRef]
126. Zhang, X.; Xia, M.; Wang, F.; Lei, W. Cu_2O/MoS_2 composites: A novel photocatalyst for photocatalytic degradation of organic dyes under visible light. *Ionics* **2020**, *26*, 6359–6369. [CrossRef]
127. Mahalakshmi, G.; Rajeswari, M.; Ponnarasi, P. Fabrication of dandelion clock-inspired preparation of core-shell $TiO_2@MoS_2$ composites for unprecedented high visible light-driven photocatalytic performance. *J. Mater. Sci. Mater. Electron.* **2020**, *31*, 22252–22264. [CrossRef]
128. Mahalakshmi, G.; Rajeswari, M.; Ponnarasi, P. Synthesis of few-layer $g\text{-}C_3N_4$ nanosheets-coated MoS_2/TiO_2 heterojunction photocatalysts for photo-degradation of methyl orange (MO) and 4-nitrophenol (4-NP) pollutants. *Inorg. Chem. Commun.* **2020**, *120*, 108146. [CrossRef]
129. Adhikari, S.; Mandai, S.; Kim, D.H. Free-standing Ag nanoparticle-decorated MoS_2 microflowers grown on carbon cloth for photocatalytic oxidation of Rhodamine, B. *Korean J. Chem. Eng.* **2020**, *37*, 2359–2367. [CrossRef]
130. Wang, Y.; Sun, S.; Liu, Y.; Zhang, Y.; Xia, J.; Yang, Q. TiO_2 coupled to predominantly metallic MoS_2 for photocatalytic degradation of rhodamine B. *J. Mater. Sci.* **2020**, *55*, 12274–12286. [CrossRef]
131. Kumaresan, N.; Karuppasamy, P.; Pandian, M.S.; Ramasamy, P. Formation of face-contact interaction in 2D/2D/2D heterostructure ternary nanocomposites of $g\text{-}C_3N_4/MoS_2/GO$ for effective photocatalytic activity against the organic pollutants under the visible light irradiation. *J. Mater. Sci. Mater. Electron.* **2022**, *33*, 11970–11988. [CrossRef]
132. Rao Akshatha, S.; Sreenivasa, S.; Parashuram, L.; Raghu, M.S.; Yogesh Kumar, K.; Madhu Chakrapani Rao, T. Visible-light-induced photochemical hydrogen evolution and degradation of crystal violet dye by interwoven layered MoS_2/Wurtzite ZnS Heterostructure Photocatalyst. *Chem. Select.* **2020**, *5*, 6918–6926.
133. Jaleel, U.C.J.R.; Devi, K.R.S.; Madhushree, R.; Pinheiro, D. Statistical and experimental studies of $MoS_2/g\text{-}C_3N_4/TiO_2$: A ternary Z-scheme hybrid composite. *J. Mater. Sci.* **2021**, *56*, 6922–6944. [CrossRef]
134. Shi, Z.; Zhang, Y.; Duoerkun, G.; Cao, W.; Liu, T.; Zhang, L.; Liu, J.; Li, M.; Chen, Z. Fabrication of MoS_2/BiOBr heterojunctions on carbon fibers as a weaveable photocatalyst for tetracycline hydrochloride 65 degradation and Cr (VI) reduction under visible light. *Environ. Sci. Nano.* **2020**, *7*, 2708–2722. [CrossRef]
135. Guo, J.; Yang, C.; Sun, Z.; Yang, Z.; Wang, L.; Lu, C.; Ma, Z.; Guo, F. Ternary $Fe_3O_4/MoS_2/BiVO_4$ nanocomposites: Novel magnetically separable visible light-driven photocatalyst for efficiently degradation of antibiotic wastewater through p–n heterojunction. *J. Mater. Sci. Mater. Electron.* **2020**, *31*, 16746–16758. [CrossRef]
136. Liu, J.; Lin, H.; He, Y.; Dong, Y.; Rose, E.; Menzembere, G.Y. Novel CoS_2/MoS_2@Zeolite with excellent adsorption and photocatalytic performance for tetracycline removal in simulated wastewater. *J. Clean. Prod.* **2020**, *260*, 121047. [CrossRef]
137. Chen, L.; Huang, C.P.; Chuang, Y.; Nguyen, T.B.; Chen, C.W.; Dong, C.D. Z-Scheme MoS_2/TiO_2/graphene nanohybrid photocatalysts for visible light-induced degradation for highly efficient water disinfection and antibacterial activity. *New J. Chem.* **2022**, *46*, 14159–14169. [CrossRef]
138. Chen, L.; Chuang, Y.; Chen, C.W.; Dong, C.D. Facile synthesis of MoS_2/ZnO quantum dots for enhanced visible-light photocatalytic performance and antibacterial applications. *Nano Struct. Nano Objects* **2022**, *30*, 100873. [CrossRef]
139. Vaizoğullar, A.İ. Ternary $CdS/MoS_2/ZnO$ photocatalyst: Synthesis, characterization and degradation of ofloxacin under visible light irradiation. *J. Inorg. Organomet. Polym. Mater.* **2020**, *30*, 4129–4141. [CrossRef]
140. Zou, X.; Zhao, X.; Zhang, J.; Lv, W.; Qiu, L.; Zhang, Z. Photocatalytic degradation of ranitidine and reduction of nitrosamine dimethylamine formation potential over MXene–Ti_3C_2/MoS_2 under visible light irradiation. *J. Hazard. Mater.* **2021**, *413*, 125424. [CrossRef]

141. Ghasemipour, P.; Fattahi, M.; Rasekh, B.; Yazdian, F. Developing the ternary ZnO doped MoS_2 nanostructures grafted on CNT and reduced graphene oxide (RGO) for photocatalytic degradation of aniline. *Sci. Rep.* **2020**, *10*, 4414. [CrossRef]
142. Wang, Y.; Tang, X.; Liu, Z.; Yan, Y.; Yang, B.; Zhu, Z. Fabrication of a Z-scheme MoS_2/CuO heterojunction for enhanced 2-mercaptobenzothiazole degradation activity and mechanism insight. *New J. Chem.* **2020**, *44*, 18264–18273. [CrossRef]
143. Sajjad, M.; Tahir, M.B.; Mubeen, I.; Kabli, M.R. Tailorable and rationally designed MoS_2 based heterostructure photocatalyst for efficient photocatalytic degradation of phenol under the visible light. *J. Inorg. Organomet. Polym. Mater.* **2020**, *30*, 3965–3972. [CrossRef]
144. Bhati, A.; Anand, S.R.; Saini, D.; Gunture, S.; Sonkar, K. Sunlight-induced photoreduction of Cr(VI) to Cr(III) in wastewater by nitrogen-phosphorus-doped carbon dots. *NPJ Clean Water* **2019**, *2*, 12. [CrossRef]
145. Kumari, A.; Chaudhary, D.R. Engineered microbes and evolving plastic bioremediation technology. *INC.* **2020**, 417–443.
146. Somasundar, Y.; Burton, A.E.; Mills, M.R.; Zhang, D.Z.; Ryabov, A.D.; Collins, T.J. Quantifying evolving toxicity in the TAML/peroxide mineralization of propranolol. *iScience* **2021**, *24*, 101897. [CrossRef]
147. Zeng, Z.; Ye, S.; Wu, H.; Xiao, R.; Zeng, G.; Liang, J.; Zhang, C.; Yu, J.; Fang, Y.; Song, B. Research on the sustainable efficacy of g-MoS_2 decorated biochar nanocomposites for removing tetracycline hydrochloride from antibiotic-polluted aqueous solution. *Sci. Total Environ.* **2019**, *648*, 206–217. [CrossRef]
148. Huang, S.; Chen, C.; Tsai, H.; Shaya, J.; Lu, C. Photocatalytic degradation of thiobencarb by a visible light-driven MoS_2 photocatalyst. *Sep. Purif. Technol.* **2018**, *197*, 147–155. [CrossRef]
149. Chandrabose, G.; Dey, A.; Gaur, S.S.; Pitchaimuthu, S.; Jagadeesan, H.; Braithwaite, N.J.; Selvaraj, V.; Kumar, V.; Krishnamurthy, S. Removal and degradation of mixed dye pollutants by integrated adsorption photocatalysis technique using 2-D MoS_2/TiO_2 nanocomposite. *Chemosphere* **2021**, *279*, 130467. [CrossRef]
150. Saleh, T.A. Trends in the sample preparation and analysis of nanomaterials as environmental contaminants. *Trends Environ. Anal. Chem.* **2020**, *28*, e00101. [CrossRef]
151. Louie, S.M.; Ma, R.; Lowry, G.V. Transformations of nanomaterials in the environment. *Front. Nanosci.* **2014**, *7*, 55–87.
152. Cicuéndez, M.; Silva, V.S.; Santos, J.; Coimbra, A.; Oliveira, H.; Ayán-Varela, M.; Paredes, J.I.; VillarRodil, S.; Vila, M. MoS_2 flakes stabilized with DNA/RNA nucleotides: In vitro cell response. *Mater. Sci. Eng. C* **2019**, *100*, 11–22. [CrossRef]